Raman spectroscopy study of manganese oxides: Tunnel structures

Jeffrey E. Post[1],*, David A. McKeown[2], and Peter J. Heaney[3]

[1]Department of Mineral Sciences, National Museum of Natural History, Smithsonian Institution, Washington, D.C., 20013-7012, U.S.A.
[2]Vitreous State Laboratory, The Catholic University of America, Washington, D.C. 20064, U.S.A.
[3]Department of Geosciences, Penn State University, 540 Deike Building, University Park, Pennsylvania 16802, U.S.A.

Abstract

Raman spectra were collected for an extensive set of well-characterized tunnel-structure Mn oxide mineral species employing a range of data collection conditions. Using various laser wavelengths, such as 785, 633, and 532 nm at low power levels (30–500 μW), as well as the comprehensive database of standard spectra presented here, it is generally possible to distinguish and identify the various tunnel structure Mn oxide minerals. The Raman mode relative intensities can vary significantly as a function of crystal orientation relative to the incident laser light polarization direction as well as laser light wavelength. Consequently, phase identification success is enhanced when using a standards database that includes multiple spectra collected for different crystal orientations and with different laser light wavelengths. For the hollandite-group minerals, the frequency of the Raman mode near 630 cm^{-1} shows a strong linear correlation with the fraction of Mn^{3+} in the octahedral Mn sites. With the comprehensive Raman database of well-characterized Mn oxide standards provided here (and available online as Supplemental Materials[1]), and use of appropriate data collection conditions, micro-Raman is a powerful tool for identification and characterization of biotic and abiotic Mn oxide phases from diverse natural settings, including on other planets.

Keywords: Manganese oxide, Raman spectroscopy, todorokite, hollandite
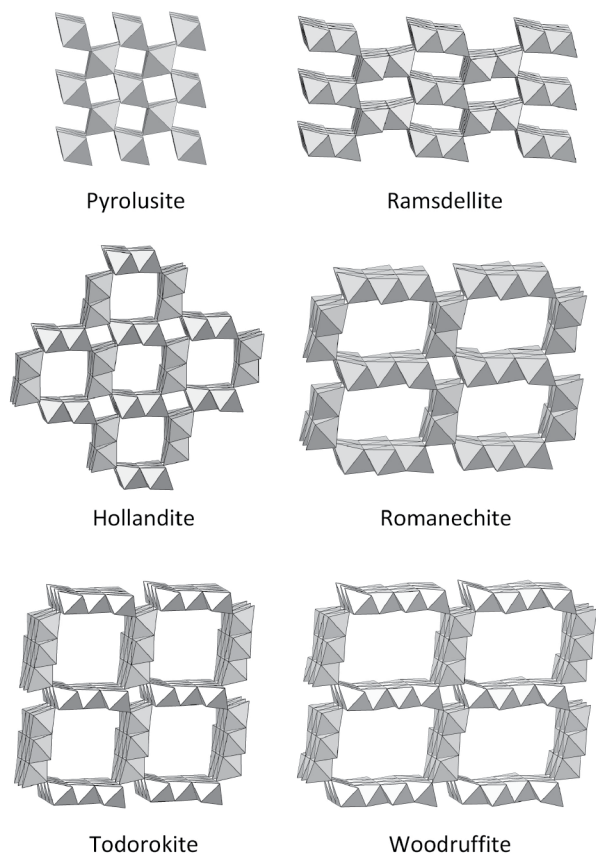
Introduction

Manganese oxide/hydroxide minerals are found in a wide variety of natural settings; they are important components of many soils and sediments and are commonly found as coatings on rocks and nodules, as well as oxidation products of Mn-rich deposits. These phases can precipitate from solution as the result of macro- or microscale changes in redox conditions, pH, or composition; additionally, studies during the past few decades have demonstrated that many Mn oxides in our environment likely form as a result of biologically mediated processes (Tebo et al. 2004; Santelli et al. 2011). Mn oxide minerals are chemically active, readily participating in redox and cation-exchange reactions. They also adsorb a large variety of metal cations, even if present in small quantities, because they commonly occur as fine-grained coatings with large surface areas. As a consequence of these properties, Mn oxides can control the metal concentrations in water associated with soils and sediments (Le Goff et al. 1996; Post 1999; Manning et al. 2002; Feng et al. 2007; Lopano et al. 2009; Kwon et al. 2013; Fleeger et al. 2013; Shumlas et al. 2016; Kong et al. 2019).

Natural Mn oxides are ubiquitous and reactive, and as a result, there is a large body of research devoted to investigating their structures and reactivities. An essential part of that work requires identification of the particular Mn oxide phases and an understanding of their behaviors to inform geochemical models for basic reactions and interactions among minerals and biologi-cal systems within the Earth's Critical Zone. Additionally, many Mn oxides are essential materials used in batteries, catalysts, molecular sieves, and numerous other industrial applications (Ghodbane et al. 2009; Li et al. 2012; Nam et al. 2015). These phases are also of interest to archeologists because of their roles in pigments, ceramics, and as age-dating tools for certain sites and artifacts (Caggiani and Colomban 2011). As a consequence of these uses and interests, characterizing Mn oxide structures and their properties under various conditions is critical.

Studies of Mn oxides are challenged by the sheer number of these species; there are more than 30 known Mn oxide/hydroxide minerals that commonly are fine-grained, poorly crystalline, and occur in the color palette of gray to brown to black, and consequently are difficult to distinguish visually in the field or in hand specimens. This great diversity of Mn oxide minerals in natural systems is in part because Mn occurs in three oxidation states (+4, +3, and +2), and because the MnO_6 octahedral building blocks can share edges, corners, or faces to construct a large variety of tunnel and layer structures (Fig. 1). Natural samples can occur as fine-scale intergrowths of two or more phases that readily alter from one to another. In many cases, X-ray diffraction (XRD) patterns exhibit broad peaks from multiple disordered phases, making basic phase identification difficult or impossible. Consequently, many researchers employ other methods in addition to XRD to characterize natural Mn oxides, such as X-ray absorption spectroscopy (XAS), Fourier transform infrared spectroscopy (FTIR), transmission electron microscopy (TEM), and combined energy-dispersive X-ray spectroscopy and scanning electron microscopy (EDS-SEM). These

* E-mail: postj@si.edu

FIGURE 1. Polyhedral drawings of manganese oxide tunnel structures.

tion tool, but also for investigating changes in response to certain redox, cation-exchange, and other reactions (Bernard et al. 1993). Additionally, current plans for the next NASA Mars lander include a Raman system, and one of the primary targets will be black rock coatings that resemble rock varnishes on Earth (Marnocha 2017). As Mn oxides in terrestrial varnishes are thought to be biologically precipitated (McKeown and Post 2001; Northup et al. 2010; Marnocha and Dixon 2014), Raman identification of similar Mn oxide minerals on Mars might be interpreted as indicators of past or possibly current biotic processes on Mars (Marnocha 2017). A comprehensive database of high-quality Raman spectra from well-characterized Mn oxide minerals will be critical to the success of such a Martian study.

The application of Raman spectroscopy to decipher Mn oxides has been invigorated in part by advances in micro-Raman technology that have resulted in wider availability of affordable in-house Raman systems. Modern instruments typically offer multiple laser options and high-sensitivity detectors that provide a range of data collection conditions that can be optimized for particular samples. Additionally, Raman spectrometers fitted with high-quality microscopes permit rapid in situ interrogation of samples with spatial resolution approaching 1 μm. These micro-Raman systems have the potential to provide phase identification and structural information quickly and easily from discrete areas on natural or synthetic Mn oxide samples. In particular, the combination of Raman microscopy and analytical SEM provides unparalleled insights into the micro mineralogy and chemistry of complex samples. Moreover, high-spatial resolution mapping is a standard capability in most new Raman instruments.

A primary advantage of the Raman technique is that the spectra provide information about local atomic coordination environments as well as longer-range structure, and therefore can be a useful identification technique even for highly disordered materials. Although Raman spectroscopy has long been used to characterize Mn oxides, previous efforts revealed serious limitations. Raman spectra from many Mn oxide phases are inherently weak, and phase changes and structural alteration can be caused by rapid heating of these opaque, dark, and highly absorbing materials when using certain laser wavelengths (Julien et al. 2004; Bernardini et al. 2019). Some older investigations were disadvantaged by the less robust technology available at the time, while others were unaware of, or ignored, problems associated with laser-heating induced changes in the samples. Several studies have reported Raman spectra for only a modest number of Mn oxide phases and samples, many of which were not phase pure. Even studies that emphasize the use of "low laser power" are inconsistent in their determinations of the instrumental conditions required to maintain specimen integrity. This issue is complicated by the effects of different laser wavelengths, power densities, and optics used for data collection. A recent overview by Bernardini et al. (2019) of the application of Raman spectroscopy to Mn oxides underscored the general promise of the approach, but this study considered a relatively limited number of samples and data collection conditions.

In the work presented here, we provide results from what we believe is the most comprehensive analysis of the Raman spectra for tunnel-structure Mn oxide phases to date. (Raman spectra of layered Mn oxides will be treated in a parallel but separate study.)

techniques also have experimental limitations and requirements, such as special sample preparation methods, large sample sizes, or synchrotron X-ray sources, and most cannot be applied to fine-scale, in situ analyses.

Because of the difficulties of working with complex natural Mn oxide samples, many researchers use synthetic phases that are presumed to be suitable analogs of the minerals. Off-setting the advantages of working with pure, relatively well-crystalline laboratory-produced samples is the difficulty of assessing their relevancy to natural phases or systems. Additionally, complexities and confusion introduced by the use of multiple synthesis methods can cause problems comparing results among different research groups.

Therefore, an improved capability to routinely identify and characterize natural Mn oxide phases, even as poorly crystalline mixtures, with minimal sample preparation, is an important step for better understanding the role of Mn oxide minerals in the environment, and for more accurate comparisons of laboratory experiments to natural systems. Micro-Raman spectroscopy is one approach that offers intriguing possibilities and is finding increased application to the study of these phases (e.g., Bernard et al. 1993; Julien et al. 2002, 2003, 2004; Hsu et al. 2011; Kim and Stair 2004; Burlet and Vanbrabant 2015; Yang et al. 2015; Bernardini et al. 2019; Boumaiza et al. 2019). During the past few decades, numerous reports have described applications of Raman spectroscopy to Mn oxides, primarily as an identifica-

Raman spectra were collected from a large number and variety of natural and synthetic samples, drawing from the Smithsonian Institution's extensive collection of Mn oxide specimens, and additional samples, which in many cases have been characterized in great detail using supplementary techniques. Raman spectra were collected using multiple Raman systems with a range of laser wavelengths to provide comparisons and determine optimal data collection conditions. Additionally, we present representative spectra from different specimens, localities, and crystal orientations. A major goal of this study is to provide a spectral database that can be used for identifying the various Mn oxide mineral phases, with an emphasis on natural samples. In turn, this work has provided insights about Mn oxide composition, crystal structure, symmetry, and in some circumstances Mn oxidation states.

EXPERIMENTAL METHODS

Specimens

The tunnel-structure Mn oxide mineral samples used in this study are listed in Table 1, including information about individual compositions. Structure symmetry and factor group analyses (Fateley et al. 1972) for the various phases are presented in Table 2. A variety of samples were included to represent variations in composition, structural disorder, and locality. All samples were checked by powder X-ray diffraction (XRD) to confirm phase identification and purity. Energy-dispersive X-ray spectroscopy (EDS) analyses and backscattered electron imaging were used to determine composition and assess chemical homogeneity. Where possible, single

crystals, or crystal fragments, were selected for Raman measurements; fine-grained samples were lightly crushed, or in some cases, prepared as polished sections that were also used for chemical analyses. For some Raman measurements, loose sample grains were placed on glass slides without adhesive, which can introduce strong luminescence.

X-ray diffraction (XRD)

Samples were characterized by powder XRD using a Rigaku II D/MAX-RAPID micro-diffractometer (Department of Mineral Sciences, Smithsonian Institution) equipped with a graphite monochromator and a curved image plate area detector. A Mo tube (50 kV, 40 mA) was used as the X-ray source with a 0.3 mm collimator. Small (~1 mm) balls of powdered samples (with added super-glue as needed), or fragments of fine-grained polycrystalline materials, were mounted on tips of glass fibers. During exposure to X-rays, the sample was rotated at 1 °/min on ϕ to minimize the effects of sample heterogeneity and preferred orientation. The full set of Debye-Scherrer diffraction rings from the imaging plate data were integrated using Rigaku-provided software, and interpretation of XRD patterns was performed using the JADE 9 software package. Phase identifications were confirmed using the ICDD PDF-4 Minerals database and an in-house collection of well-characterized Mn oxide mineral standards.

Scanning electron microscopy

Uncoated samples (which then could also be used for Raman analysis) were mounted on carbon tape adhered to an aluminum stub and analyzed with scanning electron microscopy (SEM) using a field emission source (FEI Apreo) equipped with an EDAX Octane Silicon Drift EDS detector (Department of Mineral Sciences, Smithsonian Institution). Backscattered electron (BSE) images were collected, and EDS analysis was used to determine the chemical composition and homogeneity of the Mn oxide samples (with beam current of 1.6 nA). The images were collected and analyses performed in low vacuum (0.31 torr) at an

TABLE 1. Specimens used for Raman spectroscopy

Mineral	Specimen no.	Locality	Chemical formula
Pyrolusite	149941	Kamataka, India	MnO_2
	114785-22	Amapa, Brazil	
		Sidirhal, Morocco	
	C7568	Halbinsel, Egypt	
	105572	Lake Valley, NM	
Ramsdellite	120302	Pinal Co., AZ	MnO_2
Manganite	157872	Thuringia, Hartz Mtns. Germany	$MnOOH$
Groutite	R10087	Ironton, MN	$MnOOH$
Bixbyite	151352	Postmasburg, South Africa	Mn_2O_3
Hausmannite	C6568-1	Hotazel, South Africa	Mn_3O_4
Manjiroite		Smaart Mi, South Africa	$(Na_{0.62}K_{0.40}Ca_{0.08}Mg_{0.08})(Mn_{7.90}Si_{0.10})O_{16}$
Cryptomelane	89104[a]	Chindwara, India	$(K_{0.94}Na_{0.25}Sr_{0.13}Ba_{0.10}Mg_{0.03})(Mn_{6.33}^{4+}Mn_{1.20}^{3+}Fe_{0.30}^{3+}Al_{15})O_{16}$
	2236-1	Ironwood, MI	$(K_{0.69}Ba_{0.13}Na_{0.13})(Mn_{7.67}Al_{0.30}Si_{0.03})O_{16}$
		Montreal Mi., WI	$(K_{0.54}Ba_{0.49}Pb_{0.08})(Mn_{7.61}Al_{0.39})O_{16}(Ba_{0.63}K_{0.44}Pb_{0.09})(Mn_{7.13}Al_{0.82}Si_{0.05})O_{16}$
		Virginia	$(K_{0.66})(Mn_{7.08}Al_{0.69}Si_{0.23})O_{16}\cdot nH_2O$
Hollandite	127118[a]	Ultevis, Sweden	$(Ba_{0.75}Pb_{0.16}Na_{0.10}K_{0.04})(Mn_{6.08}^{4+}Fe_{1.32}^{3+}Mn_{0.50}^{3+}Al_{0.23})O_{16}$
	93687	Michigan	$(Ba_{0.60}K_{0.37})(Mn_{7.84}Al_{0.11}Si_{0.05})O_{16}$
		Tower Mi, NM	$(Ba_{0.79}K_{0.22}Sr_{0.03})(Mn_{7.91}Al_{0.09})O_{16}$
Coronadite	AMNH 23050	Bou Tazzoult, Morocco	$(Pb_{1.06}Ba_{0.10})(Mn_{7.7}Al_{0.20}Al_{0.08})O_{16}$
	G17590	Broken Hill, Australia	$PbMn_8O_{16}$
	104685	Bou Tazoult, Morocco	$Pb_{1.44}(Mn_{7.73}V_{0.16}Al_{0.11})O_{16}$
	106257	Broken Hill, Australia	$Pb_{1.50}(Mn_{7.82}Al_{0.18})O_{16}$
	10217	Broken Hill, Australia	$Pb_{1.40}(Mn_{7.9}Al_{0.05}Zn_{0.05})O_{16}\cdot1.55H_2O$
Romanechite	R2232	Romaneche, France	$(Ba_{0.67}, H_2O_{1.33})Mn_5O_{10}$
	C1818	Schneeberg, Germany	$(Ba_{0.66}Ca_{0.03}Mg_{0.02}Na_{0.01})(Mn_{4.83}Al_{0.01}Si_{0.06}R_{0.04})O_{10}\cdot H_2O_{1.20}$ R = W, Zn, Ni, Co, Cu
	90593	Bonnet Hill, VA	$(Ba_{0.58}Ca_{0.03}K_{0.01})(Mn_{4.71}Al_{0.19}Si_{0.10})O_{10}\cdot H_2O_{1.33}$
	HU 97618	Van Horn, TX	$(Ba_{0.52}Na_{0.06}Mg_{0.06}Ca_{0.05}K_{0.04})Mn_5O_{10}\cdot H_2O_{1.30}$
Todorokite	HU 126232[b]	Smaart Mi, South Africa	$(Mg_{0.45}Na_{0.42}Ca_{0.15}K_{0.01})Mn_6O_{12}\cdot4H_2O$
	118176-13	Brazil	$(Mg_{0.37}Na_{0.25}Ca_{0.18}K_{0.02})Mn_6O_{12}\cdot4H_2O$
		Poona, India	$(Mg_{0.51}Ca_{0.28}Na_{0.13}K_{0.03})Mn_6O_{12}\cdot4H_2O$
	106238	Cuba	$(Mg_{0.51}Na_{0.37}Ca_{0.24}K_{0.04}Ba_{0.03}Sr_{0.02})Mn_6O_{12}\cdot4H_2O$
	105391	Todoroki Mi., Japan	$(Ca_{0.47}Mg_{0.13}Na_{0.12}K_{0.04})Mn_6O_{12}\cdot4H_2O$
		Medford, MD	$(Mg_{0.35}Ca_{0.34}K_{0.08})Mn_6O_{12}\cdot4H_2O$
	140503	Furnace Creek, CA	$(Na_{0.52}Ca_{0.38}Mg_{0.37}K_{0.02})(Mn_{5.91}Al_{0.09})O_{12}\cdot4H_2O$
		Yakutia, Russia	$(Na_{0.40}Ca_{0.23}Mg_{0.22}Sr_{0.10}K_{0.09})(Mn_{5.95}Al_{0.05})O_{12}\cdot4H_2O$
Woodruffite		Mapimi, Mexico[c]	$Zn_{2.8}(Mn_{8.4}^{4+}Mn_{3.6}^{3+})O_{28}\cdot9.5H_2O$
	112992	Sterling Hill, NJ	

[a] Post et al. 1982.
[b] Post et al. 2003a.
[c] Post et al. 2003b.

TABLE 2. Factor-group analysis (FGA) results of the tunnel structure-type Mn-oxides phases

Phase	Space group: Point group	FGA
Pyrolusite (MnO_2)	$P4_2/mnm$ (#136): $4/mmm$	$\Gamma_{optic} = A_{1g} + A_{2g} + B_{1g} + B_{2g} + E_g + 2B_{1u} + 3E_u$
		$\Gamma_{acoustic} = A_{2u}(z) + E_u(xy)$
Ramsdellite (MnO_2)	$Pbnm$ (#62): mmm	$\Gamma_{optic} = 6A_g + 6B_{1g} + 3B_{2g} + 3B_{3g} + 3A_u + 2B_{1u} + 5B_{2u} + 5B_{3u}$
		$\Gamma_{acoustic} = B_{1u}(z) + B_{2u}(y) + B_{3u}(x)$
Manganite [γ-MnO(OH)]	$P2_1/c$ (#14): $2/m$	$\Gamma_{optic} = 12A_g + 12B_g + 11A_u + 10B_u$
		$\Gamma_{acoustic} = A_u(z) + 2B_u(xy)$
Groutite [α-MnO(OH)]	$Pnma$ (#62): mmm	$\Gamma_{Optic} = 8A_g + 4B_{1g} + 8B_{2g} + 4B_{3g} + 4A_u + 7B_{1u} + 3B_{2u} + 7B_{3u}$
		$\Gamma_{acoustic} = B_{1u}(z) + B_{2u}(y) + B_{3u}(x)$
Hausmannite (Mn_3O_4)	$I4_1/amd$ (#141): $4/mmm$	$\Gamma_{optic} = 2A_{1g} + A_{2g} + 3B_{1g} + B_{2g} + 4E_g + 2A_{1u} + 4A_{2u} + 2B_{1u} + 4B_{2u} + 6E_u$
		$\Gamma_{acoustic} = A_{2u}(z) + E_u(xy)$
Hollandite [$Ba(Mn,Fe,Al)_8(O,OH)_{16}$]	$I2/m$: $2/m$	$\Gamma_{optic} = 13A_g + 8B_g + 8A_u + 16B_u$
		$\Gamma_{acoustic} = A_u(z) + 2B_u(xy)$
Romanechite ($Ba,H_2O)_2Mn_5O_{10}$	$C2/m$: $2/m$	$\Gamma_{optic} = 14A_g + 7B_g + 8A_u + 20B_u$
		$\Gamma_{acoustic} = A_u(z) + 2B_u(xy)$
Todorokite ($Na,Ca,K,Ba,Sr)_{0.3-0.7}(Mn,Mg,Al)_6O_{12}\cdot3.2-4.5(H_2O)$	$P2/m$: $2/m$	$\Gamma_{optic} = 16A_g + 8B_g + 10A_u + 20B_u$
		$\Gamma_{acoustic} = A_u(z) + 2B_u(xy)$
Woodruffite $Zn_{0.2}(Mn^{4+}_{0.6}Mn^{3+}_{0.4})O_2\cdot0.7(H_2O)$	$C2/c$: $2/m$	$\Gamma_{optic} = 32A_g + 19B_g + 20A_u + 34B_u$
		$\Gamma_{acoustic} = A_u(z) + 2B_u(xy)$

Notes: Γ_{optic} includes Raman- and IR-active modes; three $\Gamma_{acoustic}$ modes are indicated for each phase. The space group and point group of each phase are listed in Hermann-Mauguin notation.

accelerating voltage of 15 kV. The data were processed using the Noran System Six 3 (NSS 3) software.

Raman spectroscopy

Raman spectra were collected at 25 °C in back-scattering geometry using three single-grating spectrograph–notch filter micro-Raman systems. The first system (Smithsonian Institution, Department of Mineral Sciences) consists of a HORIBA LabRam HR Evolution equipped with a Synapse back-illuminated deep depleted, Peltier cooled 1024×128 element CCD camera. The spectra were collected using combinations of 532 and 785 nm solid state lasers, as well as 300 and 600 gr/mm spectrograph gratings, respectively, for spectral resolution near 4 cm^{-1}. An Olympus $100\times$ or $50\times$ objective was used to focus the incident laser light onto the sample. The Si 520 cm^{-1} line from a Si wafer was used for Raman frequency calibration. The laser power at the sample was measured using a Thorlabs power meter (PM100USB) for the various combinations of microscope objectives and lasers. Typically, spectra were collected using laser powers of 540 μW or less for the 532 nm laser and 350 μW or lower for the 785 nm laser. Some phases, e.g., pyrolusite, groutite, and manganite, did not exhibit obvious spectral changes at laser powers up to 2 mW, but those with larger tunnel structures, including hollandites, romanechite, and todorokite, showed evidence of sample degradation or phase transformation at laser power settings above ~500 μW. For the 532 nm laser, romanechite and todorokite spectra exhibited changes at power values as low as 300 μW. The laser power measurements are intensities at the sample, not power densities, which vary depending upon the laser spot size, determined by the objective used, laser focus, and certain other instrumental and sample surface characteristics.

The second system (Vitreous State Laboratory, Catholic University) consists of a WITec alpha-300 RA+ micro-Raman system, where 633 nm solid state diode and 532 nm DPSS lasers were used with a 600 gr/mm grating to disperse the Raman scattered light on to a 1024×128 element Peltier cooled CCD camera (Andor Technology Model DV401A-BVF-352). Zeiss objectives of $50\times$ and $100\times$ were used producing a ~1 μm laser spot size on the sample. The spectra were frequency calibrated to the Si 520 cm^{-1} mode. The spectral resolution of the data produced from these system configurations is near 6 cm^{-1}.

The third system (Vitreous State Laboratory, Catholic University) (Goncharov and Struzhkin 2003) consists of a Melles-Griot Model 45 Ar$^+$ laser that provided 457.9 and 514.5 nm wavelength light that was guided through a long working distance Mitutoyo $10\times$ microscope objective and focused to a 10 μm diameter spot on the sample. The scattered light proceeded through holographic notch and supernotch filters (Kaiser Optical Systems), which reduced the Rayleigh (or elastically) scattered light intensity by 10 optical densities. The Horiba HR460 spectrograph used a 1200 gr/mm grating (Richardson Grating Laboratory) to disperse the Stokes scattered light from the sample on to a 2048×512 element Peltier cooled CCD detector (Andor Technology Model DU440BV). Due to the relatively broad spectral features for most samples measured, the spectrograph incident slits were set to 6 cm^{-1} spectral resolution. The spectrograph was frequency calibrated using CCl$_4$, such that recorded Raman mode frequencies for all spectra are accurate to within ±1 cm^{-1} of the published values. The laser power for this system was minimized to <0.5 mW at the sample to avoid sample heating and alteration.

For each sample, initial data collection was performed using minimal laser power, e.g., 30 μW; the power level was gradually increased until noticeable changes occurred to the spectra, such as variations in peak intensities, the appearance of new peaks, or broad band luminescence with evidence of sample darkening or hole formation at the incident laser light position. Where possible, relatively flat and smooth sample surfaces, as ascertained at $100\times$ or $50\times$ magnification, were selected for data collection, using 5 to 60 s integration times per acquisition, with two to 10 acquisitions per spot to improve signal-to-noise. Crystal orientation effects were apparent for most tunnel-structure Mn oxide phases. Fibrous samples known to be elongated parallel to the octahedral chains or tunnels were placed both parallel and perpendicular to the polarization vector of the incident laser light for the series of unpolarized or polarized spectra collected. Polarized spectra were gathered using an analyzer polarizer inserted in the scattered light path. Polarized spectra were labeled vertical-vertical (VV) or vertical-horizontal (VH) to describe collection conditions where the laser light polarization was oriented parallel or perpendicular, respectively, to the polarization direction of the analyzer. For comparison, unpolarized spectra also were collected without an analyzer in the scattered light path between the sample and spectrograph.

Lattice dynamics calculations

To provide overall guidance for some general vibrational assignments to the observed Raman features, preliminary normal coordinate valence-force lattice dynamics (LD) calculations at zero wavevector (Dowty 1987, 2007) were performed for the 2×2 tunnel hollandite structure as well as the 2×3 tunnel romanechite structure. The models included Mn-O stretch as well as O-Mn-O bend force constants to simulate the various bonding environments within the linked MnO_6 octahedra. Tunnel cation-oxygen stretch force constants were also included. The force constants were allowed to vary so that the calculated mode frequencies best matched the set of observed mode frequencies from the Raman spectra for each phase.

Overall, LD calculations indicate that Raman-active modes for these two Mn-oxides can be divided into three frequency ranges. Above 500 cm^{-1}, modes are dominated by Mn-O stretch as well as O-Mn-O bend motions within MnO_6 octahedra. Modes between 100 and 500 cm^{-1} are due to less localized mixtures of MnO_6 translation, rotation, deformation, and shear displacements. Below 100 cm^{-1}, modes are dominated by displacements of heavy cations within the tunnels, such as Pb^{2+} in hollandite and Ba^{2+} in romanechite. Mixtures of these atomic displacement types are found for calculated modes between 100 and 500 cm^{-1}.

RESULTS

MnO$_2$-pyrolusite and ramsdellite

Pyrolusite and ramsdellite are MnO_2 polymorphs, and in natural samples they can occur as intergrowths (e.g., in the mineral nsutite) and as pyrolusite pseudomorphs after ramsdellite. Pyrolusite has the rutile structure, i.e., $Mn^{4+}O_6$ octahedra share

edges to form chains, which share corners to form a tetragonal structure having tunnels with square cross sections, measuring one octahedron on a side (Fig. 1). The tunnels are too small to accommodate cations, other than possibly H^+, and therefore, most natural pyrolusite samples are close to the ideal composition. Ramsdellite has the diaspore structure, where the $Mn^{4+}O_6$ octahedra share edges to form double chains, which link corners to form tunnels with one octahedron by two octahedra cross-sections (Fig. 1). Again, the small tunnels are mostly unoccupied, except for H^+ in some samples.

The Raman spectra for pyrolusite and ramsdellite are shown in Figures 2 and 3, respectively. The prominent vibrational modes with frequencies in the range 450 to 760 cm^{-1} are common features for most Mn oxides; they have been interpreted by various researchers as Mn-O stretch and bending modes arising from the $Mn^{4+}O_6$ octahedra (Julien et al. 2004; Bernardini et al. 2019, and others). As $Mn^{4+}O_6$ is the basic building block of most Mn oxide phases, these Raman lines can be diagnostic for many of the Mn oxides, but as the $Mn^{4+}O_6$ bonding environments are similar in many of these structures, these Raman modes alone might not be diagnostic of a specific phase. The overall structural symmetry, and that of the octahedral Mn site, determines the number, frequencies, and relative intensities of the vibrational

modes in this frequency range, as does the Mn oxidation state, particularly in the case of Jahn-Teller distorted $Mn^{3+}O_6$ octahedra.

Pyrolusite and ramsdellite spectra collected using 532, 633, and 785 nm lasers are generally similar for a given phase, although Raman intensities collected with the 785 nm laser are significantly weaker. These phases also are relatively robust in terms of withstanding different laser power levels; for 532 and 785 nm lasers, there were no significant changes observed in the Raman spectra until incident laser powers exceeded 2 mW at the sample. Above these thresholds, the appearance of a strong mode at 630 cm^{-1} indicates a phase transformation to a hausmannite-like phase (Fig. 4). Although the overall Raman spectrum for the laser altered phase resembles that of hausmannite, the position of the major peak at 630 cm^{-1} is shifted from that of 655 cm^{-1} observed for our standard hausmannite (Fig. 5). This difference suggests that the laser-heated pyrolusite might transform to a non-stoichiometric hausmannite, or possibly, the frequency shift is due to small crystallite sizes of the hausmannite (Xu et al. 2005).

The spectra in Figures 2 and 3 for pyrolusite and ramsdellite, respectively, were collected from individual crystals where fibers (elongated parallel to the octahedral chains) were aligned parallel or perpendicular to the polarization of the incident laser beam. Internal MnO_6 octahedral Mn-O stretch and O-Mn-O bend
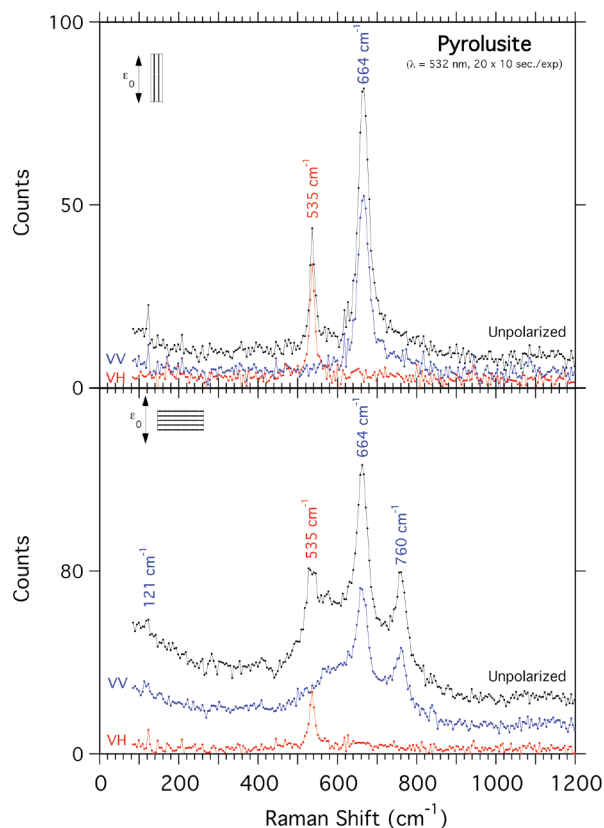
FIGURE 2. Raman spectra for pyrolusite (India no. 149941) using a 532 nm laser with crystals (elongated along tunnels) oriented parallel (top) and perpendicular (bottom) to laser light polarization. Spectra labeled VV and VH were collected using parallel and crossed polarization conditions, respectively. (Color online.)
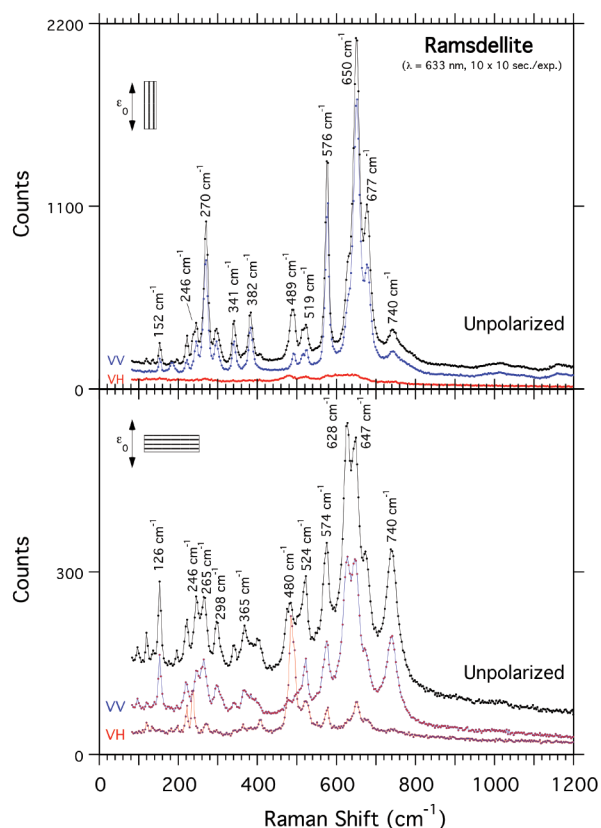
FIGURE 3. Raman spectra (633 nm) for ramsdellite (Arizona no. 120303) with crystals (elongated along tunnels) oriented parallel (top) and perpendicular (bottom) to laser light polarization. Spectra labeled VV and VH were collected using parallel and crossed polarization conditions, respectively. (Color online.)

modes, above 500 cm^{-1}, show significant intensity changes at these different crystal orientations. With respect to these orientation effects, it is important to note that natural pyrolusite samples commonly occur as euhedral acicular crystals, such that Raman spectra from "powder" samples using focused laser spots approaching 1 μm actually represent individual crystals, or oriented crystal bundles. Consequently, at these collection conditions, relative intensities of some spectral features can be quite variable due to crystal orientation.

Porto et al. (1967) determined that for rutile, which is isostructural with pyrolusite, there are four Raman-active phonon modes predicted by factor-group analysis (FGA): A_{1g}, B_{1g}, B_{2g}, and E_g. Our pyrolusite Raman spectra look similar to those shown by Porto et al. (1967), and by analogy to rutile, we have assigned these modes in the pyrolusite spectra in Figure 2. Lan et al. (2012) carried out molecular dynamical simulations for the rutile structure and determined that the sharp, lowest frequency B_{1g} mode was related to a rotating motion of the four nearest-neighbor oxygen atoms around the Ti atom (Mn in pyrolusite), and that the A_{1g} mode arose from metal–oxygen stretch motions perpendicular to the c-axis, and the E_g mode from metal–oxygen stretch motions parallel to c. The Raman spectra for pyrolusite (Fig. 2) using parallel and crossed polarization conditions confirm that the 535 cm^{-1} peak must correspond to the asymmetric E_g mode and the intense band at 664 cm^{-1} to the A_{1g} mode. The highest frequency mode calculated by Porto et al. (1967) for rutile is B_{2g}, a metal-O stretching mode that presumably corresponds to the Raman peak observed for pyrolusite at 740–760 cm^{-1}. This mode is most obvious when the pyrolusite c-axis is oriented perpendicular to the incident laser light polarization direction and therefore arises from Mn-O stretch motions perpendicular to the tunnel direction, i.e., axial octahedral bonds. Because the Mn-O octahedral bond distances (1.882–1.894 Å) are shorter (and stiffer) than those for Ti-O (1.965 Å) (Shannon 1976), the A_{1g} and E_g Raman-active modes for pyrolusite are shifted to higher frequencies relative to those for rutile.

Bernardini et al. (2019) observed for pyrolusite an additional Raman peak at 585 cm^{-1} that appeared at increased power using green laser light, which was attributed to the transformation of pyrolusite to bixbyite (Mn_2O_3). Our Raman spectra for bixbyite (Fig. 6), however, did not exhibit any strong features near 585 cm^{-1}. We observed weak to moderate intensity peaks at ~575 cm^{-1} for some of our pyrolusite samples, but the appearance and intensity of the peak did not change with increased laser power. One explanation is that the peak arises from intergrowths of ramsdellite, which has a strong peak near 575 cm^{-1} (Fig. 3). Powder XRD patterns for natural pyrolusite commonly show small amounts of ramsdellite.

Factor-group analysis (Fateley et al. 1972) for the ramsdellite structure (space group *Pnma*) indicates 18 Raman modes (Table 2), consistent with the more complex ramsdellite Raman spectrum (Fig. 3), relative to that of pyrolusite. In particular, the larger number of peaks in the internal octahedral MnO$_6$ (Mn-O stretch and O-Mn-O bend) mode region reflect the lower symmetry of the Mn-O octahedral environment (four unique Mn-O distances, vs. only two in pyrolusite). DFT modeling of the
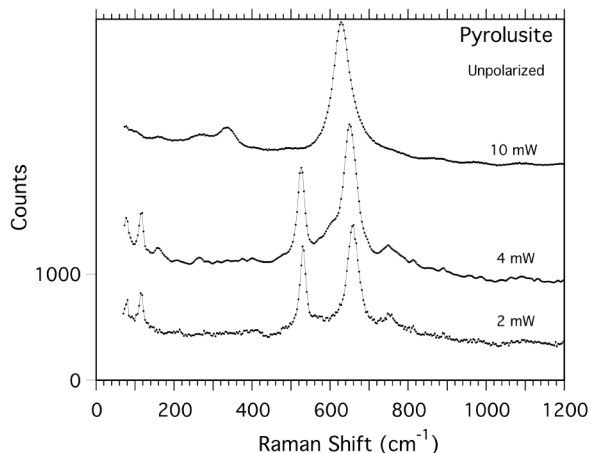

Figure 4. Raman spectra (532 nm) for pyrolusite (Brazil no. 114785-22) at power levels on the sample of 2, 4, and 10 mW.
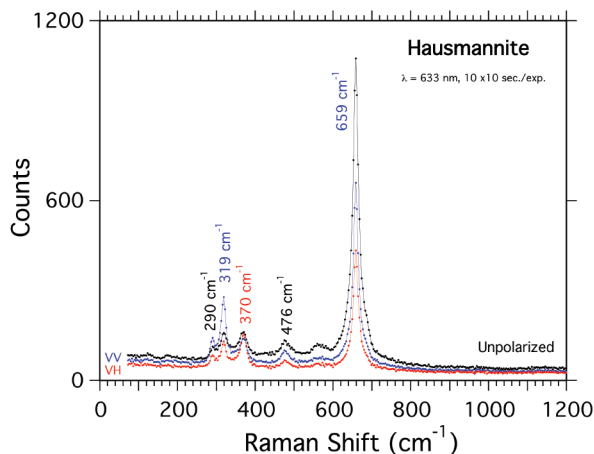

Figure 5. Raman spectra (633 nm) for hausmannite (S. Africa no. 168527). Spectra labeled VV and VH were collected using parallel and crossed polarization conditions, respectively. (Color online.)
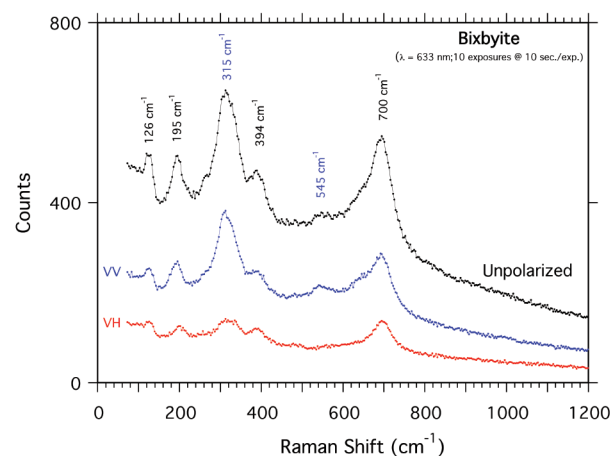

Figure 6. Raman spectra (633 nm) for bixbyite (S. Africa no. 151352). Spectra labeled VV and VH were collected using parallel and crossed polarization conditions, respectively. (Color online.)

diaspore (AlOOH) structure (Delattre et al. 2012) revealed that the Raman peaks below 1000 cm^{-1} are lattice modes, involving the deformation or relative displacement of AlO_6 octahedra; this implies similar lattice modes for MnO_6 in ramsdellite within this frequency range.

Mn(OOH)–manganite and groutite

Manganite is isostructural with pyrolusite, and groutite with ramsdellite, but in each case with Mn^{3+} instead of Mn^{4+}, and OH^- replacing one-half of the O atoms. The Jahn-Teller Mn^{3+} cation gives rise to greatly distorted $Mn^{3+}O_6$ octahedra for both phases and lower overall symmetry for manganite ($P2_1/c$) compared with pyrolusite ($P4_2/mnm$). Upon heating, both phases transform into pyrolusite, and natural samples of manganite commonly contain pyrolusite.

The Raman spectra for manganite and groutite are shown in Figures 7 and 8, respectively. The spectra were collected from individual crystals for which the tunnel directions were aligned parallel or perpendicular to the polarization direction of the laser beam. These spectra show significant intensity changes with different crystal orientations for some of the Raman lines, particularly in the internal octahedral MnO_6 mode region, above 500 cm^{-1}.

Group theory predicts 12 A_g and 12 B_g modes for manganite, and Figure 7 shows the more complex Raman spectrum for manganite relative to pyrolusite (Fig. 2). Manganite has six Mn-O octahedral distances, compared with two for pyrolusite (1.88 and 1.89 Å), and the Jahn-Teller distortion yields a range of distances from 1.88 to 2.34 Å. The internal octahedral MnO_6 mode region between 500 and 760 cm^{-1} for manganite shows at least four modes that are shifted to lower frequencies with respect to the pyrolusite Raman modes, reflecting the longer average Mn-O distances relative to pyrolusite.

Groutite has the same symmetry as ramsdellite ($Pnma$), but has six more Raman active modes due to the additional OH (Table 2); the internal octahedral MnO_6 modes are shifted to lower frequencies because of Mn^{3+}. Also, the ramsdellite spectra show peaks between 740 and 760 cm^{-1} that are absent for groutite (Figs. 3 and 8). The groutite spectra collected under parallel and crossed polarization conditions reveal that the Mn-O stretch modes between 500 and 650 cm^{-1} are A_g modes (symmetric), and those at 97, 385, and 485 cm^{-1} are B_g modes (asymmetric) (Fig. 8). Presumably, the mode at 1065 cm^{-1} in the groutite spectra, but absent for ramsdellite, is related to OH^- in groutite. This interpretation is consistent with studies of the Raman spectra for the isostructural disapore (AlOOH) (Delattre et al. 2012) that noted OH bending modes at 1045 and 1188 cm^{-1}. As this band is strongest when groutite crystals are oriented such that the tunnel direction is parallel to the polarization direction of the incident laser light, we conclude that this mode represents OH bending with motion in the tunnel direction. XRD studies (Kohler et al. 1997) confirm that the OH bond is perpendicular to the tunnel direction; and therefore, an Mn-OH stretch mode would be most prominent for a crystal fiber perpendicular to the incident laser light polarization.

Hollandite-group minerals

Minerals with the hollandite structure are constructed of double chains of Mn-O octahedra, as in ramsdellite, but the chains link corners to form a structure containing tunnels with
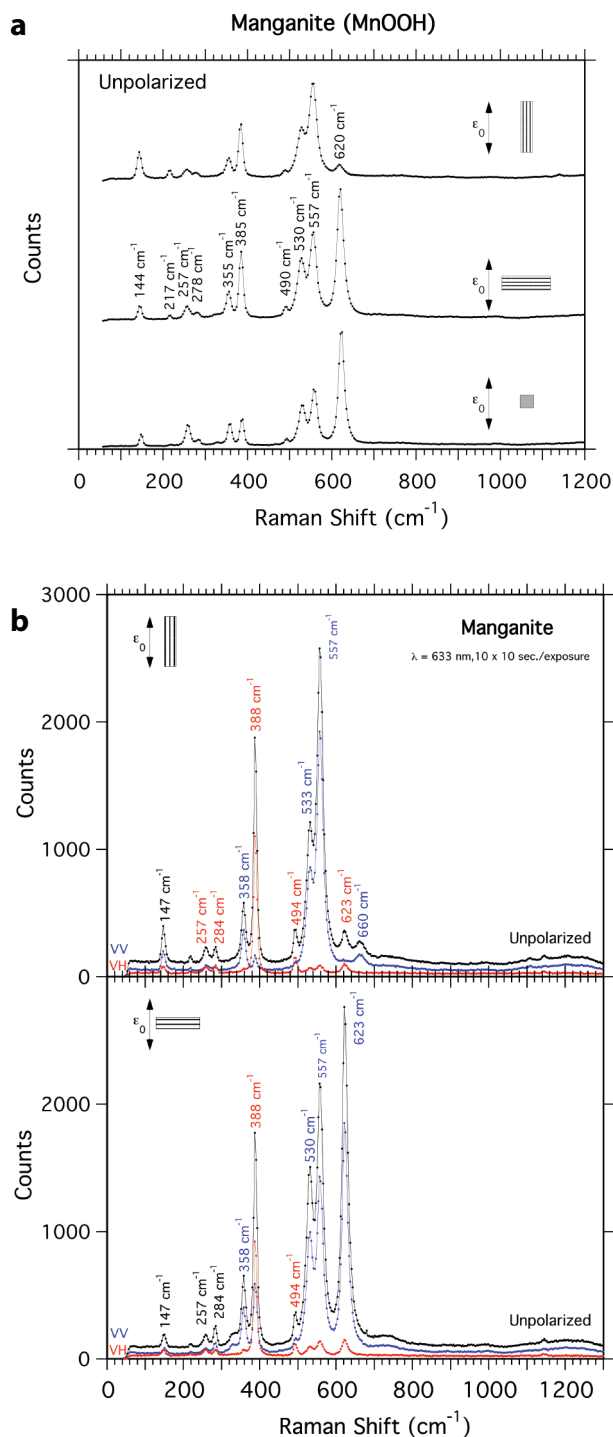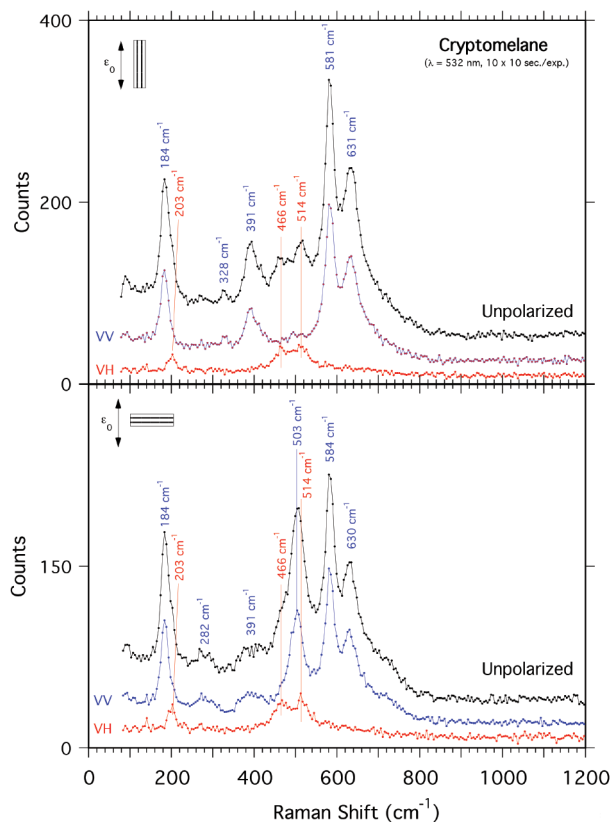

FIGURE 7. Raman spectra for (**a**) manganite (Germany no. 157872) using 532 nm laser with crystals (elongated along tunnels) oriented parallel (top) and perpendicular (middle) to laser light polarization, and with crystal tunnel direction oriented parallel to the laser beam direction, and (**b**) (633 nm) with crystal oriented with tunnels parallel (top) and perpendicular (bottom) to laser light polarization; spectra labeled VV and VH were collected using parallel and crossed polarization conditions, respectively. (Color online.)
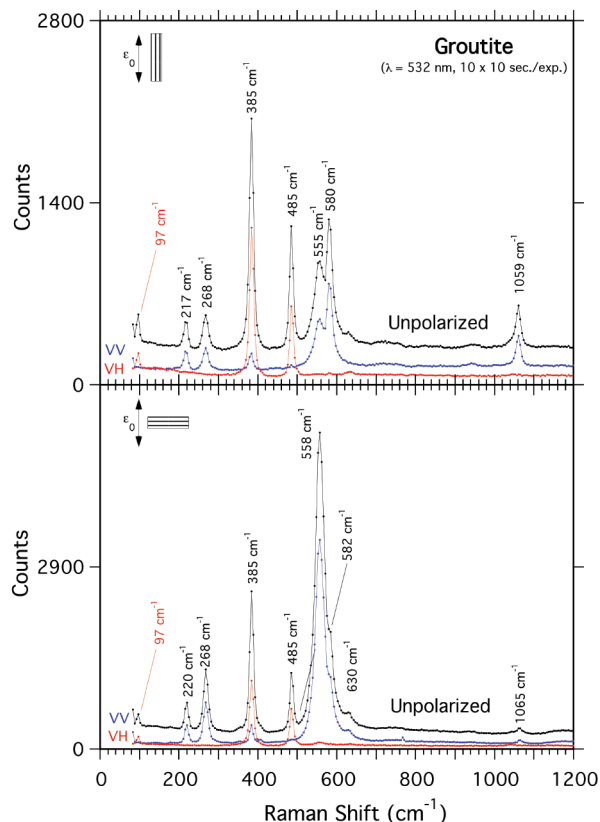
FIGURE 8. Raman spectra (532 nm) for Groutite (MN no. R10087) with crystals (elongated along tunnels) oriented parallel (top) and perpendicular (bottom) to laser light polarization. Spectra labeled VV and VH were collected using parallel and crossed polarization conditions, respectively. (Color online.)

FIGURE 9. Raman spectra (532 nm) for cryptomelane (India no. 89104) with crystals (elongated along tunnels) oriented parallel (top) and perpendicular (bottom) to laser light polarization. Spectra labeled VV and VH were collected using parallel and crossed polarization conditions, respectively. (Color online.)

square cross-sections that are two octahedra on a side (Fig. 1). These large tunnels can accommodate various uni- and divalent cations as well as some water molecules, where the charges on these tunnel cations are offset by substitution of lower valence cations, typically Mn^{3+}, Al^{3+}, and Fe^{3+}, for the Mn^{4+} in the octahedral framework. The predominant tunnel cation determines the particular mineral: hollandite (Ba^{2+}), cryptomelane (K^+), strontiomelane (Sr^{2+}), coronadite (Pb^{2+}), and manjiroite (Na^+), but pure end-members are rare in nature so that most samples contain mixtures of two or more types of tunnel cations. The chemistry of these minerals is also complicated in that they typically have Mn in two oxidation states along with other cations in the octahedral sites. In natural hollandite-like phases, the fraction of Mn^{3+}/Mn^{4+} generally ranges from 0.10 to 0.25, depending on the charges and quantities of tunnel cations, as well as the presence of other lower valence cations in the octahedral sites. There are two distinct Mn sites, one with Mn^{4+} and the other with Mn^{3+}. Most hollandite minerals are pseudo-tetragonal with monoclinic symmetry ($I2/m$).

The Raman spectrum for a cryptomelane from India, used for the single-crystal X-ray diffraction study by Post et al. (1982), is shown in Figure 9. As all hollandite-group minerals have the same basic octahedral framework, their Mn-O bonding environments,

and therefore corresponding Raman modes, will be comparable, with minor variations caused by the fraction of Mn^{3+}/Mn^{4+} and accompanying Jahn-Teller distortions, substitutions of other octahedral cations, replacement of some O^{2-} by OH^-, and to a lesser degree by influences of the types and numbers of tunnel cations. Not surprisingly, then, the Raman spectra are similar for the various hollandite minerals (Fig. 10). The spectra in Figure 9 were collected from individual prismatic cryptomelane crystals for which the tunnel directions were aligned parallel or perpendicular to the polarization direction of the incident laser beam. They show significant intensity changes for some of the Raman lines, particularly in the internal octahedral MnO_6 mode region. Similar variations of intensity with orientation were observed for the other hollandite phases. At laser powers above 2 mW, a peak appears at ~650 cm^{-1}, likely corresponding to hausmannite as the cryptomelane structure is transformed by the laser heating.

Lattice dynamic calculations for the hollandite structure (Fig. 11) indicate that modes above 100 cm^{-1} are due to motions within the MnO_6 octahedra as well as longer range motions among linked octahedra that form the 2 × 2 tunnels. Therefore, the spectral similarities for all the hollandite phases are not surprising. Calculated modes due to tunnel cation motions at or below 100 cm^{-1} may not be easily observed in some spectra con-
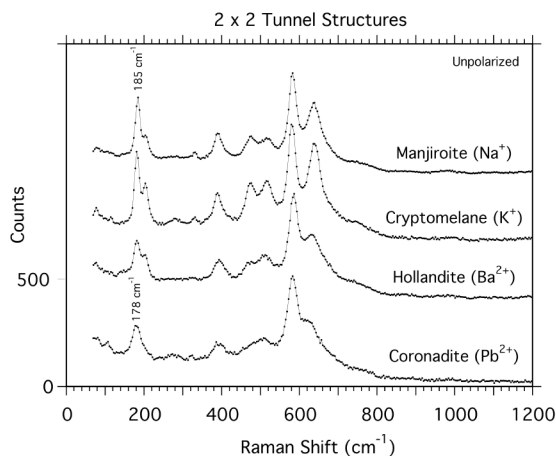
sidering the low frequency cut-offs of notch or edge filters typically used in Raman systems as well as possible strong Rayleigh scattering amplitudes commonly seen at these low frequencies. Therefore, it is also not surprising that earlier studies mentioned

FIGURE 10. Raman spectra (532 nm) for manjiroite (S. Africa), cryptomelane (no. 2236-1), hollandite (NM), and coronadite (no. 106257). The crystal elongation directions were oriented parallel to the incident beam polarization.

only subtle effects from the tunnel cations in the Raman spectra of these phases (Gao et al. 2008; Polák et al. 2017).

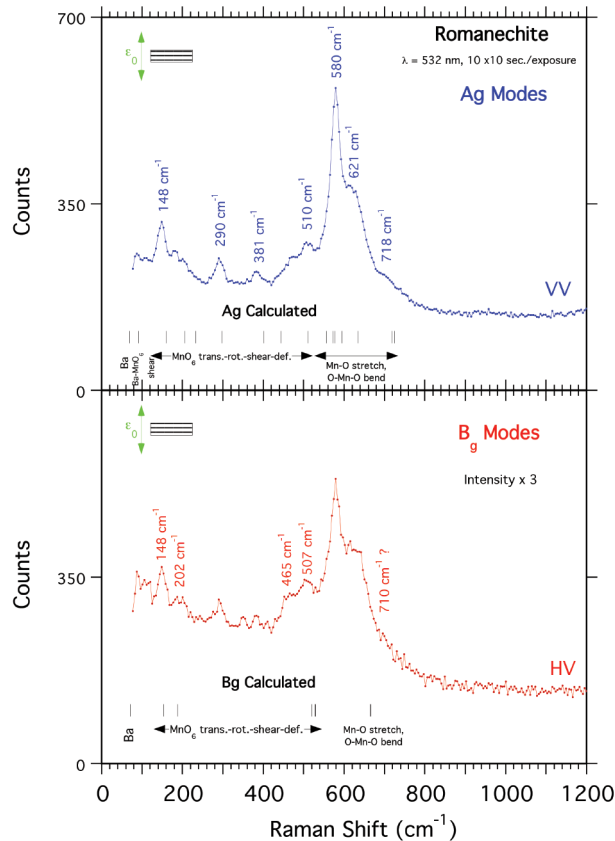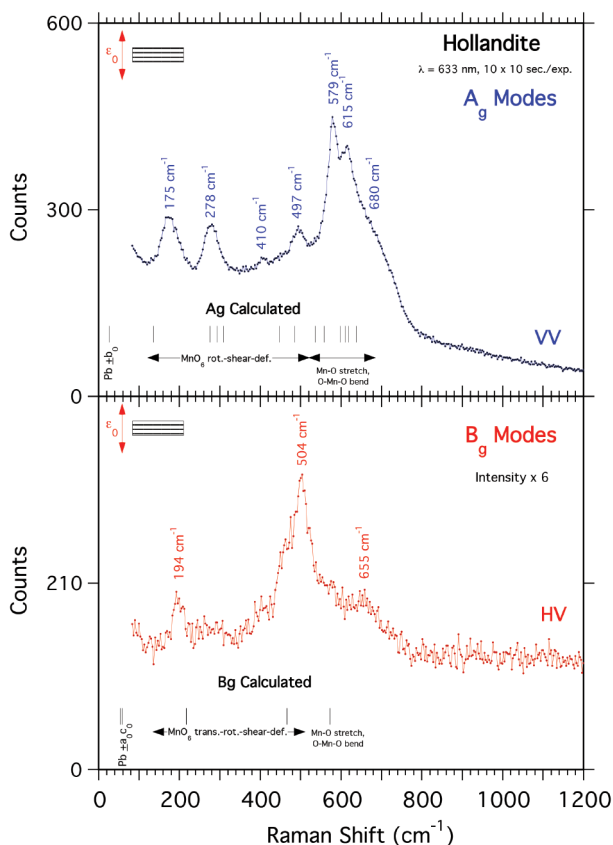### Romanechite

Romanechite is a hydrated Ba manganese oxide that consists of double and triple chains of Mn-O octahedra that link corners to form large tunnels with rectangular cross sections that measure two by three octahedra on the sides (Fig. 1). Most botroyoidal, compact natural Mn oxide mineral specimens labeled "psilomelane" are romanechite. The tunnels are filled with an ordered arrangement of Ba^{2+} cations and water molecules in a ratio of 1:2. Romanechite samples exhibit little compositional variation, with only minor substitution of K^+, Na^+, Ca^{2+}, and Mg^{2+} for Ba^{2+}. The charges on the tunnel cations are offset by Mn^{3+} replacing approximately 27% of the Mn^{4+}. Single-crystal XRD studies of the romanechite structure confirmed the $C2/m$ space group and indicated that the larger Jahn-Teller Mn^{3+} cations concentrate in the octahedra at the edges of the triple chains (Turner and Post 1988).

Raman spectra for romanechite are shown in Figure 12. As the romanechite octahedral framework is similar to that of the hollandite-group minerals (both have the same $C2/m$ symmetry but with 2×3 rather than 2×2 tunnels), their Mn-O bonding environments and corresponding Raman modes are comparable. In particular, the Raman spectra in the internal octahedral MnO_6 mode region above 500 cm^{-1} are similar to those of the hollandite

FIGURE 11. Raman modes determined using normal coordinate valence-force lattice dynamics (LD) calculations for (left) hollandite (no. 127118) and (right) romanechite (France no. R2232) plotted as vertical lines below their respective Raman spectra (633 nm). (Color online.)
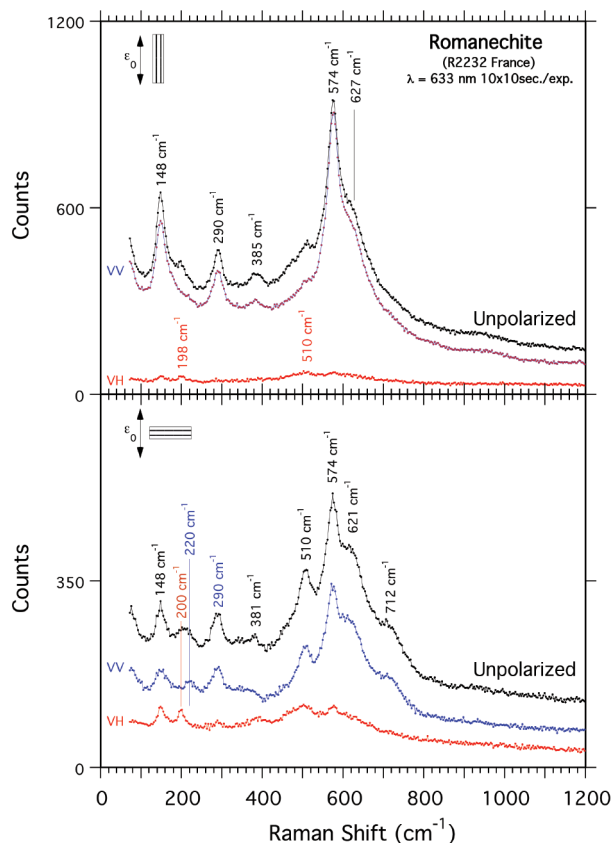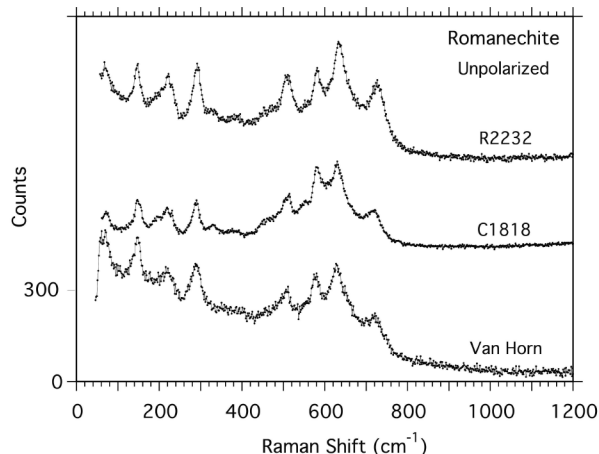
FIGURE 12. Raman spectra (633 nm) for romanechite (France no. R2232) with crystals (elongated along tunnels) oriented parallel (top) and perpendicular (bottom) to laser light polarization. Spectra labeled VV and VH were collected using parallel and crossed polarization conditions, respectively. (Color online.)

FIGURE 13. Raman spectra (785 nm) for romanechite specimens from three different localities. Spectra for R2232 and C1818 were collected using a 100x objective from individual crystals, and for Van Horn from a massive specimen with crystals smaller than 0.5 µm.

FIGURE 14. Raman spectra for romanechite (Germany no. C1818) collected using four different laser light wavelengths. (Color online.)
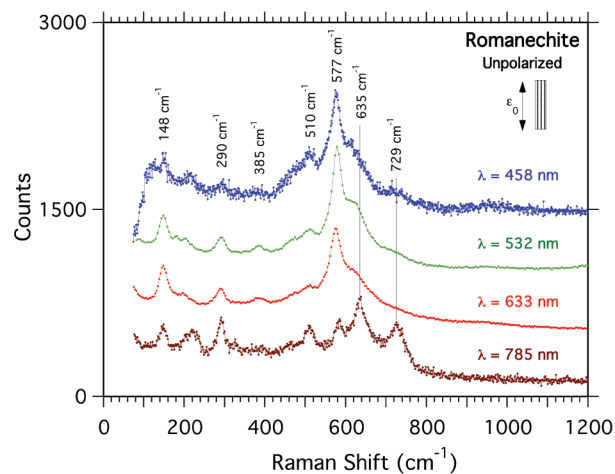
minerals (Figs. 9 and 10). The spectra in Figure 12 were collected from individual prismatic romanechite crystals for which the tunnel directions were aligned parallel or perpendicular to the polarization direction of the laser beam. They show intensity changes for some of the Raman lines, particularly in the internal octahedral MnO_6 mode region, but to a lesser degree than for the hollandite phases. Figures 13 and 14 show Raman spectra for several natural romanechite specimens from various localities, and compare romanechite spectra collected at 458, 532, 633, and 785 nm laser wavelengths. The major differences among the spectra are apparent for the 785 and 633 nm laser wavelengths, where the intensity ratio for the 635 and 577 cm^{-1} peaks is reversed and the intensity of the 730 cm^{-1} peak is diminished for the 633 nm wavelength. Raman spectra collected successively from the same sample spot using the 532 nm and then the 785 nm lasers confirm that the differences in the spectra are not caused by laser induced sample changes, but rather are due to different Raman responses from the various laser wavelengths.

Todorokite

Todorokite is a hydrated manganese oxide that consists of triple chains of Mn-O octahedra that link corners to form large tunnels with square cross se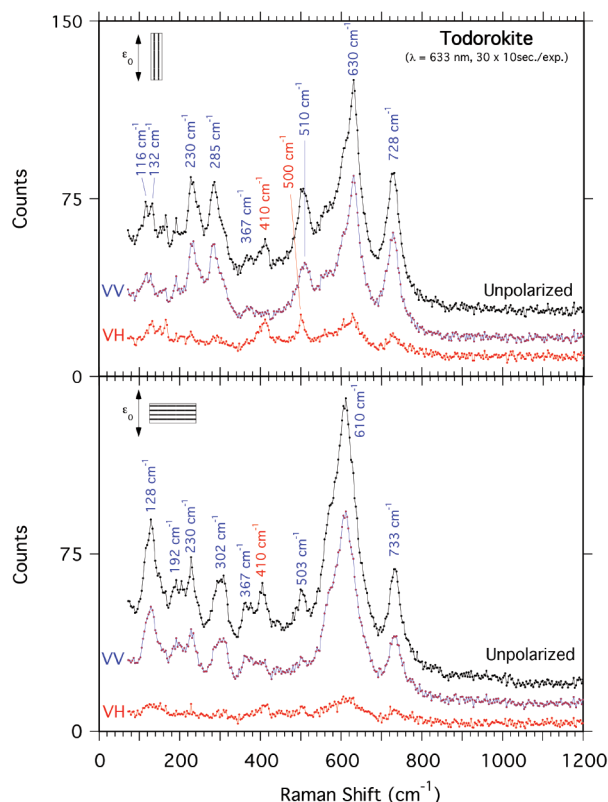ctions that measure three octahedra on a side (Fig. 1). Todorokite is a common phase in ocean manganese nodules, oxidized zones of Mn-rich ore deposits, and in dendrites, as well as in rock varnishes (McKeown and Post 2001). The large tunnels are filled with various cations, including Mg^{2+}, Ca^{2+}, Na^+, K^+, and Sr^{2+}, as well as water molecules. The charges on the tunnel cations are compensated by Mn^{3+} replacing approximately 25–33% of the Mn^{4+} in the tunnel walls, depending upon the charges and quantities of tunnel cations. Powder XRD studies of the todorokite structure confirmed the $P2/m$ space group and indicated that the larger, Jahn-Teller distorted Mn^{3+} octahedra concentrate at the edges of the triple chains (Post et al. 2003b).

The Raman spectra for todorokite from South Africa, used for the XRD study by Post et al. (2003b), are shown in Figure 15. As the todorokite octahedral framework is similar to those in romanechite and hollandite-group minerals, the nearest–neighbor Mn-O bonding environments, and corresponding Mn-O stretch and O-Mn-O bending Raman modes above 500 cm^{-1},

are comparable (Figs. 9, 12, and 15). The spectra (Fig. 15) were collected from individual prismatic todorokite crystals for which the tunnel directions were aligned parallel or perpendicular to the laser light polarization direction. Raman spectra for natural todorokite specimens from various localities that represent a range of tunnel cation compositions (Fig. 16 and Table 1) are similar, with major differences being peak broadening due to structural disorder (primarily with respect to chain-widths) in some of the samples. Spectra collected at 532, 633, and 785 nm (Fig. 17) reveal that even at very low laser power (<30 μW), the 532 nm spectrum peaks in the 500 to 750 cm^{-1} interval are broadened and the 740 cm^{-1} peak intensity is greatly diminished or absent, presumably as a result of laser heating-induced structural degradation, or possible effects of resonance enhancement by the longer wavelength laser light. Spectra collected above 350 μW using the 785 nm laser show significant changes; most obvious are broadening of features between 550 to 700 cm^{-1} and reduced intensity for the 740 cm^{-1} peak.

Woodruffite

Woodruffite is a hydrated zinc manganese oxide that consists of triple and quadruple chains of Mn-O octahedra that link corners to form the largest known (3 × 4) tunnels of any natural Mn oxide with rectangular cross sections (Post et al. 2003a).

Woodruffite is associated with oxidized zones of Zn- and Mn-rich ore deposits. The large tunnels are filled with Zn^{2+} and water molecules, where charges on the tunnel cations are offset by Mn^{3+} replacing approximately 40% of the Mn^{4+}. Single-crystal XRD studies of the woodruffite structure confirmed the $C2/m$ space group and indicated that the larger Mn^{3+} cations concentrate in Jahn-Teller distorted octahedra at the edges of the quadruple chains (Post et al. 2003a).

Raman spectra collected using the 532 and 633 nm incident wavelengths for woodruffite from Mapimi, Mexico, used for the XRD study by Post et al. (2003a), are shown in Figure 18; the 785 nm incident laser light data suffered from luminescence and are not included here. As with todorokite, the octahedral framework is similar to that of romanechite and the hollandite-group minerals; and as a result their nearest–neighbor Mn-O bonding environments and corresponding Raman modes are comparable. The spectra in Figure 18 were collected from individual prismatic woodruffite crystals for which the tun-
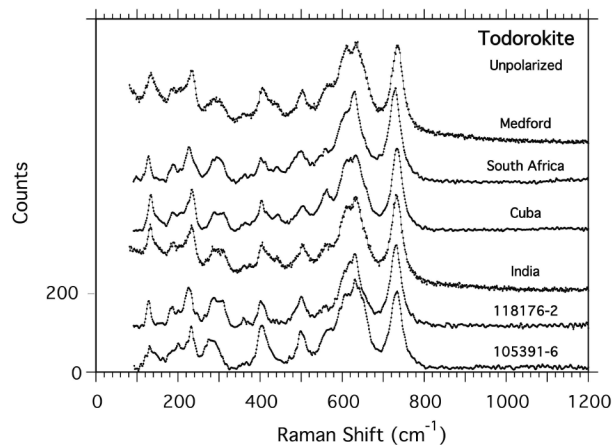
FIGURE 16. Raman spectra (785 nm) for a variety of different todorokite specimens. Locations and specimen numbers are indicated (see Table 1).
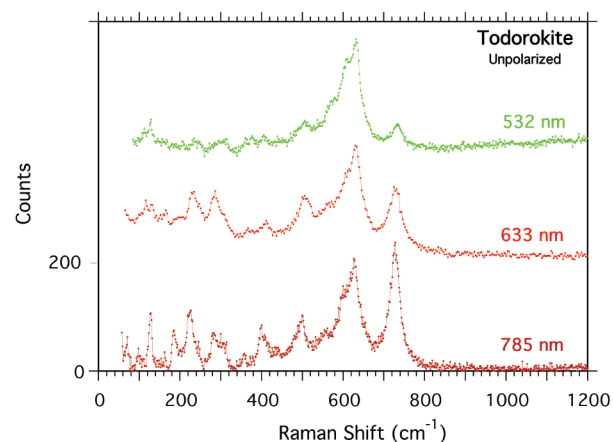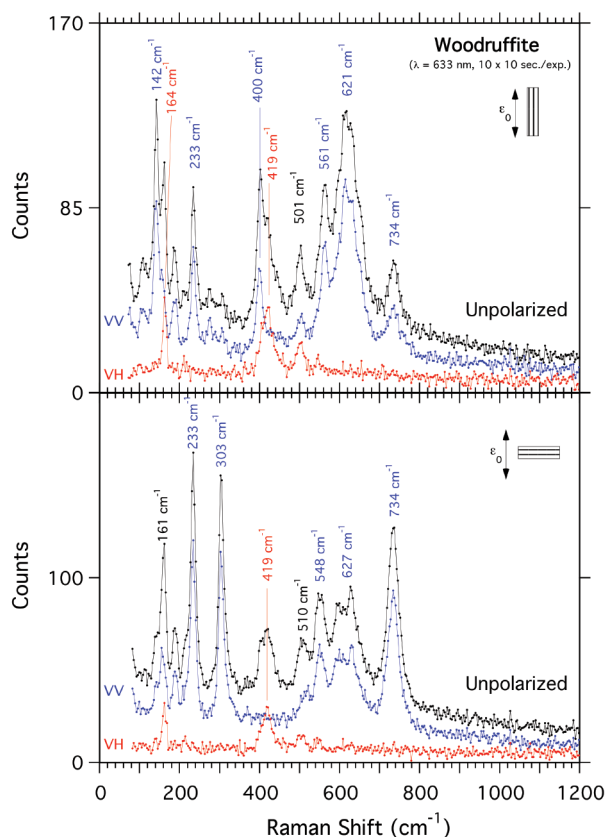

FIGURE 15. Raman spectra (633 nm) for todorokite (S. Africa no. HU126232) with crystals (elongated along tunnels) oriented parallel (top) and perpendicular (bottom) to laser light polarization. Spectra labeled VV and VH were collected using parallel and crossed polarization conditions, respectively. (Color online.)

FIGURE 17. Raman spectra for todorokite (S. Africa no. HU126232) collected using 532 (0.03 mW), 633 (<0.1 mW), and 785 (0.11 mW) nm laser light. (Color online.)

Figure 18. Raman spectra (633 nm) for woodruffite (Mexico) with crystals (elongated along tunnels) oriented parallel (top) and perpendicular (bottom) to laser light polarization. Spectra labeled VV and VH were collected using parallel and crossed polarization conditions, respectively. (Color online.)

nel directions were aligned parallel or perpendicular to the polarization of the laser beam. They show significant intensity differences for some of the Raman lines, particularly for the 736 cm^{-1} peak. Raman spectra for woodruffite collected at 532 and 633 nm laser wavelengths also show significant variations, where one major difference is the relatively lower intensity of the 734 cm^{-1} peak in the 532 nm spectrum.

DISCUSSION

In a recent study that explored the application of Raman spectroscopy for identification of Mn oxide phases, Bernardini et al. (2019) observe that "Raman spectroscopy, although widely used for the recognition of MnO$_x$, can offer ambiguous results because of literature data that are often conflicting and contradictory." Additionally, they conclude that "proper identification of the Mn-species in the sample only based on Raman spectroscopy is clearly difficult." For example, these authors assert that Raman spectroscopy cannot distinguish todorokite from cryptomelane, nor hollandite from romanechite. Indeed, unambiguous identification of many Mn oxides using Raman spectroscopy can be challenging because most phases have similar Mn-O octahedral building blocks. The Raman stretch-bending modes arising from the central octahedral Mn and the six coordinating O atoms will

be similar for many of the phases (Julien et al. 2004). The positions and relative intensities of some of these modes, however, are affected by the Mn oxidation state, which not only changes the average Mn-O distance [Mn^{4+}-O = 1.88 Å; Mn^{3+}-O = 2.04 Å (Shannon 1976)], but also the octahedral distortion, for example, in the case of Jahn-Teller effects associated with the Mn^{3+} cation. Additionally, the polymerization of the octahedra into single, double, and triple chains, and differences in long-range structural symmetry, give rise to variations in the Raman spectra that can be valuable for phase identification.

Based on our observations, we argue that it generally *is* possible to identify most unknown Mn oxide tunnel structures, at least to the level of the particular structure type (e.g., 2 × 2 vs. 2 × 3 tunnel dimensions) when using high-quality reference spectra collected under properly constrained conditions. Good signal-to-noise ratios in Raman spectra can be obtained for these phases using laser powers less than 300 μW. Although we obtained serviceable spectra for pyrolusite, manganite, ramsdellite, groutite, and most hollandite-group phases using laser wavelengths of 532, 633, and 785 nm, the stronger Raman signal produced with the 532 and 633 nm wavelengths significantly reduced the data collection times. Choice of laser wavelength, however, also depends upon minimizing sample luminescence, if present.

Care must be taken to account for spectral differences for the same phase based upon incident laser light energy. For example, the spectra collected for romanechite, todorokite, and woodruffite using the 532 nm laser typically exhibited fewer and broader peaks, suggesting structural disordering from laser heating, even when the laser power was as low as 30 μW, or a weaker Raman response for that laser wavelength. The more detailed spectra for these phases obtained with the 633 nm, and especially, the 785 nm laser wavelengths can assist with phase identification.

In addition, crystal orientation effects can dramatically change the relative intensities of specific Raman modes for many of these phases. The positions of the lines generally remained constant, but the appearance of some modes depended upon crystal orientation relative to the laser light polarization. These effects were most significant for highly crystalline samples. The use of lower resolution gratings (e.g., 300 gr/mm) can reduce the magnitude of the orientation effect for some samples, and generally yield higher intensities and adequate resolution for most Mn oxides. Collecting reference spectra for multiple crystal orientations, and to low frequencies (~100 cm^{-1}), can greatly assist with the identification of certain phases. We discuss below some of the more useful identifying spectral features for different Mn oxide phases based on our study.

Mn oxides and hydroxides

Bernardini et al. (2019) concluded that pyrolusite, manganite, hausmannite, and manganosite have sufficiently characteristic Raman spectra as to make identification of these phases straightforward, assuming the spectra are collected under low laser power conditions. We would add groutite, ramsdellite, and bixbyite to that list. Pyrolusite and manganite commonly occur together in mineral specimens, as do groutite and ramsdellite, but these phases are easily distinguished by their Raman spectra (Figs. 2 vs. 7, and 3 vs. 8).

Hollandite-group minerals

Raman spectra for several hollandite-group minerals are shown in Figure 10. As noted above, the spectra for hollandite, cryptomelane, and coronadite are similar, and they share several features that can be used to distinguish this structural group from other tunnel geometries without ambiguity: (1) a moderately strong peak at ~182 cm^{-1} is a marker for hollandite-group phases; comparable peaks occur in spectra for romanechite and todorokite, but at ~150 and 130 cm^{-1}, respectively; (2) three octahedral MnO$_6$ modes near 631, 579, and 515 cm^{-1}, with the 579 peak being most intense; (3) a moderately intense peak at 386 cm^{-1}; and (4) a moderate to weak peak at ~738 cm^{-1}. Polák et al. (2017) and Polverejan et al. (2004) attributed the 182 cm^{-1} mode to translational motion of the MnO$_6$ octahedra; we concur from observation and preliminary lattice dynamics calculations that this mode is a longer-range structural vibration, and suggest it arises from flexing of the overall octahedral framework, as the position and intensity of this peak is relatively insensitive to the tunnel cation composition or the fraction of octahedral Mn^{3+}. This assignment is also supported by the presence of similar Raman peaks for romanechite and todorokite at discrete and constant frequencies for these particular phases, and the observation that the frequencies of these peaks decrease as the tunnel sizes increase. Presumably the larger tunnel structures are less rigid with relatively weaker bonding, and as a result, associated atomic displacements have lower frequency Raman modes.

Although the Raman spectra for hollandite-group minerals are generally similar, close inspection of the spectra for hollandite, cryptomelane, and coronadite reveals subtle but distinct differences that might be used to identify the particular species. It is also important to note that the Raman spectra for several samples from different localities for each of the three phases were virtually identical to each other, indicating that the differences observed in Figure 10 are characteristic of the particular minerals (and compositions) and not simply random variations arising from different sample textures, crystallite sizes, or preparation methods. For example, the intensity of the 631 relative to the 579 cm^{-1} peak in the cryptomelane (and manjiroite) spectra is consistently greater than the intensities of those equivalent features in the hollandite and coronadite spectra. Polverejan et al. (2004) and Gao et al. (2008) similarly suggested that the relative intensities of these peaks can be used to characterize tunnel species.

Due to the substitution of Mn^{3+} for up to 25% of the Mn^{4+} in hollandite-group Mn oxides, the octahedral double chains will have both Mn^{3+} and Mn^{4+} octahedra, which have different Mn-O distances and distortions. Additionally, Mn^{4+} octahedra adjacent to a Mn^{3+} octahedron will be distorted differently than one with only Mn^{4+} nearest neighboring octahedra. Consequently, the Raman internal octahedral MnO$_6$ modes will reflect contributions from the different Mn octahedral environments, affecting the widths and intensities of the associated Raman peaks. Substitution of other trivalent cations, such as Al^{3+}, Fe^{3+}, and V^{3+}, into these octahedral sites will also influence the peak position and broadening. In Figure 10, the peak near 631 cm^{-1} is shifted to lower frequencies for hollandite and coronadite, compared with cryptomelane. We propose that the frequency of this mode correlates with the fraction of Mn^{3+} in the framework octahedral sites; the larger Mn^{3+} cation causes longer average Mn-O distances and Jahn-Teller distortions of the MnO$_6$ octahedra, primarily lengthening the axial, relative

to the equatorial, Mn-O distances. The fact that the position of the 580 cm^{-1} peak is the same for all of the hollandite-group phases suggests that the 631 cm^{-1} peak arises primarily from axial Mn-O stretch vibrations, and that its frequency decreases as the Mn^{3+}/Mn^{4+} fraction increases.

K$^+$ is the dominant tunnel cation in cryptomelane, although natural samples invariably contain quantities of other cations, such as Ba^{2+}, Na$^+$, and Sr^{2+}. Chemical analyses of synthetic and natural cryptomelanes typically show tunnel site occupancies of 1 to 1.5 cations (nominally K$^+$) per eight octahedral sites, resulting in a total tunnel cation charge of approximately +1 to +1.5 (or slightly greater if Ba^{2+} and/or Sr^{2+} are present) (Table 1). The tunnel cation charge is typically offset by substitution of the necessary amount of Mn^{3+} (with possibly some Al^{3+}, Fe^{3+}, etc.) in the octahedral sites. The Mn^{3+}/Mn$_{tot}$ value for a cryptomelane with 1.0 K$^+$ per unit cell will be 0.125, and with 1.5 K$^+$ per unit cell this ratio will be 0.188. The Mn^{3+}/Mn$_{tot}$ values calculated (from analyses to charge balance tunnel cations) for our cryptomelane samples ranged from 0.10 to 0.17 (Table 1). For hollandite (Ba) and some coronadite (Pb) samples, analyses indicated approximately 1.0 tunnel cation per unit cell; this limit for hollandite is imposed by the charge repulsion between neighboring Ba^{2+} tunnel cations that requires Ba to be spaced every other unit cell along the tunnels. Therefore, total tunnel cation charges for hollandites and some coronadites is +2, such that Mn^{3+}/Mn$_{tot}$ is ~0.25 to offset the positive charge. Our analyses revealed that some coronadites contain up to 1.5 Pb^{2+} per unit cell (Table 1); Pb^{2+} is significantly smaller than Ba^{2+}, and structure refinements (Post and Bish 1989) show that Pb displaces away from the cation site at (000) along the tunnels to permit greater occupancy. For these high-Pb coronadite samples, Mn^{3+}/Mn$_{tot}$ is ~0.34. In the present study, the position of the ~631 cm^{-1} peak exhibited a near-linear dependence on the Mn^{3+}/Mn$_{tot}$ ratio for all hollandite-type phases (Fig. 19), suggesting that the position of this peak may be used to estimate the Mn^{3+} content in 2 × 2 tunnel structures.

Romanechite

As compositions of natural romanechite samples depart only slightly from the ideal formula with tunnel sites having ⅓ Ba^{2+} and ⅔ H$_2$O (Turner and Post 1988), the Raman spectra likewise are similar for mineral samples from different localities. Additionally, the dependence of the Raman spectra on crystal orientation was minimal compared with that observed for the hollandite-group minerals. Consequently, a single Raman reference spectrum (e.g., Figs. 12 and 13) should suffice to identify romanechite. One caveat, however, is that the Raman peak intensities in spectra collected using a 785 nm laser differed significantly from those generated by 458, 532, or 633 nm laser wavelengths (Fig. 14). The peak frequencies were the same, but the relative intensities of the 580 and 634 cm^{-1} peaks were reversed. Additionally, the 785 nm spectrum showed a moderate to strong peak at 729 cm^{-1} that is weak in the other spectra shown in Figure 14. All romanechite spectra, however, exhibited a peak at ~147 cm^{-1} that can serve as an identifying marker to distinguish this phase from hollandite-group and todorokite minerals. Other useful spectral features for identifying romanechite include: (1) the moderately intense 729 cm^{-1} peak (using 785 nm laser light), which is very weak for hollandite-group phases but very strong (typically at 740 cm^{-1}) for todorokite; and (2) a strong peak near 290 cm^{-1}.

In romanechite, the overall charge from the ~0.67 Ba^{2+} tunnel
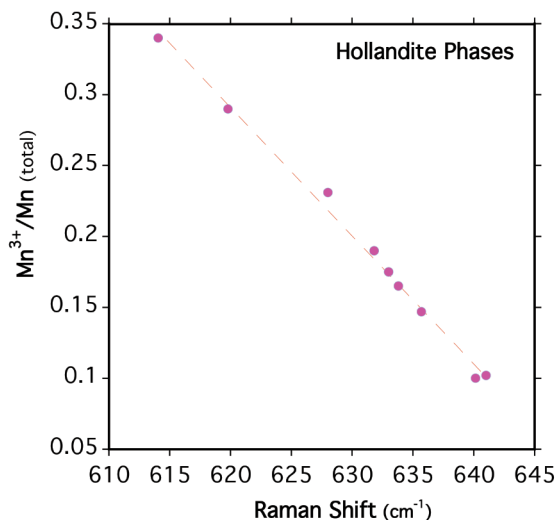
Figure 19. Plot of Mn^{3+}/Mn_{total} vs. frequency of the "630 cm⁻¹" Raman peak for various hollandite group minerals. Cryptomelane and manjiorite plot to the lower right, and hollandite and coronadite to the upper left. Linear fit equation: $y = -5.9021 - 0.0090499x$ (R = 0.99713). (Color online.)

cations per unit cell is offset by substitution of approximately 27% Mn^{3+} into the framework octahedra. Therefore, similar to the hollandite phases, the romanechite structure offers multiple MnO_6 octahedral environments, and the potential for Mn^{3+} substitution into either double and triple octahedral chains, makes the situation even more complex. The single-crystal XRD study by Turner and Post (1988) revealed three symmetrically distinct Mn sites in romanechite: (1) Mn octahedra at the edges of the triple chains where they corner link to double chains, with Mn-O distances ranging from 1.91 to 2.12 Å; (2) octahedra in the middle of the triple chains with Mn-O distances from 1.90 to 1.92 Å; and (3) Mn octahedra in the double chains, which corner link to the triple chains, having Mn-O distances from 1.87 to 1.93 Å. The range of bond distances within the octahedral sites at the edges of the triple chains indicates a Jahn-Teller distortion, revealing that ~50% of those octahedra are occupied by Mn^{3+}. Any remaining Mn^{3+} is randomly distributed in the octahedra making up the double chains. The shorter and more regular bond distances observed in the octahedra in the middle of the triple chains indicate that these sites contain only Mn^{4+}. Therefore, as with the hollandite spectra, the many Mn octahedral environments in romanechite affect the widths and intensities of the Raman modes internal to the MnO_6 octahedra.

Todorokite and woodruffite

The todorokite structure is constructed of triple Mn-O octahedral chains similar to those found in romanechite. A structure refinement by Post et al. (2003b) showed that, as with romanechite, the MnO_6 octahedra at the edges of the triple chains have longer average Mn-O distances than those in the middle of the chains, and these edge octahedra exhibit Jahn-Teller distortions consistent with the presence of Mn^{3+}. The chemical formulas for the various todorokite samples used in this study typically include an assortment of tunnel cations: Ca^{2+}, Mg^{2+}, Ba^{2+}, K^+, Na^+, and sometimes Sr^{2+}, where the total tunnel cation charge ranges from

+1.3 to +2. Similar to romanechite and the hollandite minerals, the tunnel charges are primarily offset by substitution of Mn^{3+} into the framework octahedra, perhaps with some Al^{3+}. The Mn^{3+} makes up approximately 28% of the total Mn. Todorokite, then, has three different Mn octahedral environments: (1) Mn^{4+} in the middle of the triple chains (33%), (2) Mn^{4+} at the edges of the triple chains (39%), and (3) Mn^{3+} at the edges of the triple chains (28%). As above, $Mn^{4+}O_6$ octahedra at the edges of the triple chains will be different if they are adjacent to Mn^{3+} rather than Mn^{4+}. Additional variations are likely caused by substitution of OH^- for some of the framework O atoms and H-bonding between tunnel water molecules and framework O atoms.

Previously reported Raman spectra for todorokite collected using 532 or 633 nm laser wavelengths (even at relatively low laser powers such as 0.5 mW) characteristically are dominated by a single broad peak or envelope near 630 cm⁻¹, thereby challenging the utility of this technique in the identification of todorokite (e.g., Julien et al. 2004; Bernardini et al. 2019). Julien et al. (2004) collected Raman spectra with 10 mW 532 nm laser light; the 532 nm spectrum in Figure 17 collected at ~30 μW shows additional weak-to-moderate intensity peaks near 735 and 130 cm⁻¹. When using 785 nm laser light, these peaks were more prominent, and numerous additional peaks appeared (Figs. 15–17), offering a more diagnostic spectrum for positively identifying todorokite. In particular, the peak near 720 cm⁻¹ in the 785 nm laser light spectrum exhibited weak-to-moderate intensities using 532 nm laser light (and was absent when the 532 nm laser power was greater than 30 μW), but has approximately equal intensity to that of the 630 cm⁻¹ peak for the 785 nm laser light spectrum. The 633 nm spectra for todorokite (Fig. 15) show little polarization dependent behavior, except for mode near 410 cm⁻¹. Raman spectra were collected for six natural todorokite samples from different localities (Fig. 16) and with a range of tunnel cation compositions and crystallite sizes (as indicated from powder XRD) (Table 1). The overall similarities of the spectra support the idea of a unique "standard" Raman spectrum that can be used to identify todorokite phases.

A comparison of the Raman spectra of crytomelane, romanechite, and todorokite revealed several characteristic features for todorokite (Fig. 20). In the 785 nm laser light spectra, the intensity of the peak near 740 cm⁻¹ was nearly equal to that of the peaks centered near 635 cm⁻¹. The romanechite spectra have a similar peak, but the intensity was typically about ⅓ of that for the 635 cm⁻¹ peak, and was shifted to ~725 cm⁻¹. As noted above, the longer-range structural mode peak near 125 to 132 cm⁻¹ distinguished todorokite from the romanechite and hollandite-group minerals, which have comparable peaks at higher frequencies; this peak was clearly observed in all todorokite sample spectra (e.g., Fig. 16), and it also was evident in spectra collected using 532 or 633 nm laser light at low power (below 0.1 mW). Furthermore, internal MnO_6 modes at 635 and 610 cm⁻¹ were displaced to lower frequencies relative to comparable peaks in the hollandite and romanechite spectra. Todorokite commonly is difficult to differentiate from layered Mn oxides on the basis of powder XRD patterns, but a peak in the range between 725 and 740 cm⁻¹ (Figs. 16 and 20) is not observed for birnessite-like phases, or other layer Mn oxides (unpublished results). Moreover, this peak was weak to absent in the hollandite-group spectra, and when present, merged into a high-frequency shoulder on the peak near 645 cm⁻¹. In the 785 nm

laser light romanechite spectra, this mode appeared as a moderate intensity peak near 725 cm^{-1}, but its intensity never exceeds $\frac{1}{3}$ of that of the 645 cm^{-1} peak. Weak to moderate features in this same frequency range were observed in spectra for pyrolusite and ramsdellite, but not for manganite and groutite.

This ~730 cm^{-1} peak is the highest frequency internal MnO_6 mode measured, likely arising from the shortest and strongest Mn^{4+}-O bonds. As mentioned in the Results section, Porto et al. (1967) assigned a comparable peak for rutile as a B_{2g} metal-O stretching mode that presumably corresponds to the peak observed for isostructural pyrolusite at 742 cm^{-1}. The assumption that this mode is related to Mn^{4+}-O stretch vibrations in MnO_6 octahedra is consistent with its presence in spectra for pyrolusite and ramsdellite, which contain only Mn^{4+}. This Mn valence dependent assignment also was supported by the absence of this peak in the isostructural Mn^{3+} phases manganite and groutite. Additionally, the intensities of the peaks correlate with the fractions of Mn^{4+} octahedra that are located in the centers of the triple chains, i.e., 0% for hollandite minerals, 20% for romanechite, and 33% for todorokite. Structure refinements (Turner and Post 1988; Post et al. 2003b) show that these central octahedra have the shortest Mn-O distances, consistent with occupancy by Mn^{4+}. Mode assignments for this and other Raman modes await confirmation by DFT or other lattice dynamics simulations.

Not surprisingly, the Raman spectra for the 3 × 4 tunnel structure woodruffite are similar to those for todorokite. The triple and quadruple Mn-O octahedral chains in woodruffite consist of five different octahedral environments: $Mn^{4+}O_6$ (centers of triple chains), $Mn^{3+}O_6$, and $Mn^{4+}O_6$ (edges of chains), and $Mn^{4+,3+}O_6$ in centers of the quadruple chains. The shortest Mn-O distances are in octahedra at the centers of the triple chains (Post et al. 2003a). Similar to todorokite, the spectra for woodruffite (Fig. 18) show little polarization dependent behavior, except for modes near 164 and 419 cm^{-1}. Figure 21 shows spectra for todorokite compared with those for woodruffite specimens from Mexico and Sterling Hill, New Jersey. Powder X-ray diffraction patterns and high-resolution transmission electron microscope images (unpublished results) show that the Sterling Hill woodruffite is significantly more disordered than the Mexican specimen. The todorokite and woodruffite

spectra can be roughly distinguished by frequency distributions of modes, especially under 300 cm^{-1} (see Figs. 15, 16, 18, and 21).

IMPLICATIONS

We present here a comprehensive study of Raman spectra for tunnel Mn oxide phases collected from a large assortment of well-characterized natural samples, using various data collection conditions (Fig. 22). We have demonstrated that when using multiple lasers, especially at 785 and 633 nm wavelengths, and at low incident powers (30–500 μW, depending upon the laser light wavelength and the sample), we are able to identify tunnel Mn oxide phases for most samples. With the comprehensive Raman database of well-characterized Mn oxide standards, provided here and as supplementary[1] data with the *American Mineralogist*, and use of appropriate data collection conditions, micro-Raman is a powerful tool for identification and characterization of biotic and abiotic Mn oxide phases from diverse natural settings (including on other planets), and thereby can provide new insights into the roles of these phases in our environment.
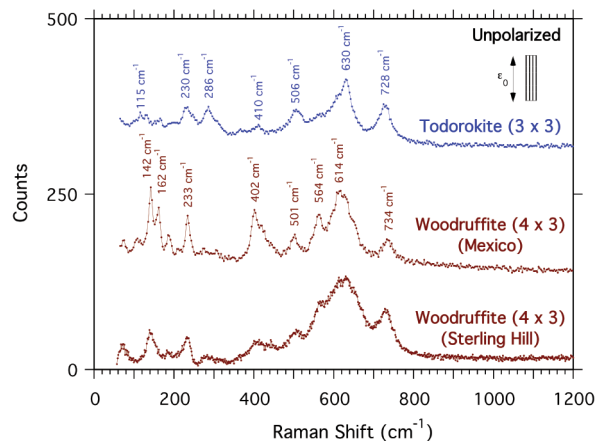
FIGURE 21. Raman spectra for todorokite (633 nm; no. HU126232) and woodruffite samples from Mexico (633 nm) and Sterling Hill, N.J. (785 nm). (Color online.)
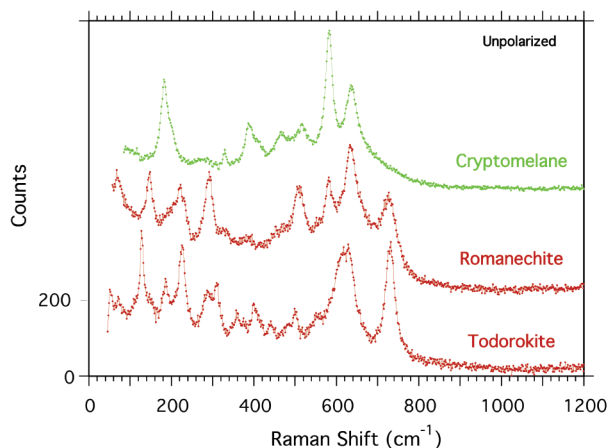
FIGURE 20. Raman spectra for cryptomelane (532 nm; no. 89104), romanechite (785 nm; R2232), and todorokite (785 nm; no. 118176-13). (Todorokite rescaled × 4.5.) (Color online.)
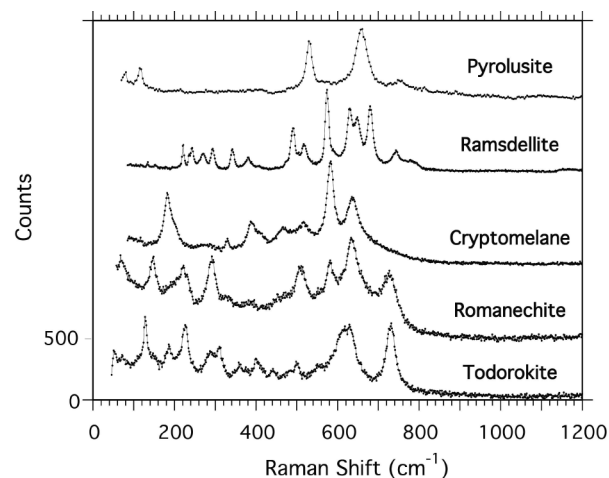
FIGURE 22. Raman spectra for a variety of Mn oxide tunnel structures using 785 nm incident laser light.

REFERENCES CITED

Bernard, M., Hugot-Le Goff, A., and Thi, B.V. (1993) Electrochromic reactions in manganese oxides. Journal of the Electrochemical Society, 140, 3065–3070.

Bernardini, S., Bellatreccia, F., Municchia, A.C., Ventura, G.D., and Sodo, A. (2019) Raman spectra of natural manganese oxides. Journal of Raman Spectroscopy, 1–16.

Boumaiza, H., Renard, A., Robinson, M.R., Kervern, G., Vidal, L., Ruby, C., Bergaoui, L., and Coustel, R. (2019) A multi-technique approach for studying Na triclinic and hexagonal birnessites. Journal of Solid State Chemistry, 272, 234–243.

Burlet, C., and Vanbrabant, Y. (2015) Study of the spectro-chemical signatures of cobalt–manganese layered oxides (asbolane–lithiophorite and their intermediates) by Raman spectroscopy. Journal of Raman Spectroscopy, 46, 941–952.

Caggiani, M.C., and Colomban, J. (2011) Testing of Raman spectroscopy as a non-invasive tool for the investigation of glass-protected pastels. Journal of Raman Spectroscopy, 42, 790–798.

Delattre, S., Balan, E., Lazzeri, M., Blanchard, M., Guillaumet, M., Beyssac, O., Haussühl, E., Winkler, B., Salje, E.K.H., and Calas, G. (2012) Experimental and theoretical study of the vibrational properties of diaspore (α-AlOOH). Physics and Chemistry of Minerals, 39, 93–102.

Dowty, E. (1987) Vibrational interactions of tetrahedra in silicate glasses and crystals. Physics and Chemistry of Minerals, 14, 122–138.

——— (2007) Vibratz2.0 software details available at: "www.shapesoftware.com".

Fateley, W.G., Dollish, F.R., McDevitt, N.T., and Bentley, F.F. (1972) Infrared and Raman Selection Rules for Molecular and Lattice Vibrations: The correlation method. Wiley.

Feng, X.H., Zhai, L.M., Tan, W.F., Liu, F., and He, J.Z. (2007) Adsorption and redox reactions of heavy metals on synthesized Mn oxide minerals. Environmental Pollution, 147(2), 366–373.

Fleeger, C.R., Heaney, P.J., and Post, J.E. (2013) A time-resolved X-ray diffraction study of Cs exchange into hexagonal H-birnessite. American Mineralogist, 98, 671–679.

Gao, T., Glerup, M., Krumeich, K., Nesper, R., Fjellvåg, H., and Norby, P. (2008) Microstructures and spectroscopic properties of cryptomelane-type manganese dioxide nanofibers. Journal of Physical Chemistry C, 112, 13,134–13,140.

Ghodbane, O., Pascal, J.L., and Favier, F. (2009) Microstructural effects on charge-storage properties in MnO₂-based electrochemical supercapacitors. Applied Materials and Interfaces, 2009, 1(5), 1130–1139.

Goncharov, A.F., and Struzhkin, V.V. (2003) Raman spectroscopy of metals, high-temperature superconductors and related materials under high pressure. Journal of Raman Spectroscopy, 34, 532–548.

Hsu, Y.K., Chen, Y.C., Lin, Y.G., Chen, L.C., and Chen, K.H. (2011) Reversible phase transformation of MnO₂ nanosheets in an electrochemical capacitor investigated by in situ Raman spectroscopy. Chemical Communications, 47, 1252–1254.

Julien, C., Rangan, S., Lemal, M., and Guyomard, D. (2002) Study of structural defects in γ-MnO₂ by Raman spectroscopy. Journal of Raman Spectroscopy, 33, 223–228.

Julien, C., Massot, M., Baddour-Hadjean, R., Franger, S., Bach, S., and Pereira-Ramos, J.P. (2003) Raman spectra of birnessite manganese dioxides. Solid State Ionics, 159(3-4), 345–356.

Julien, C.M., Massot, M., and Poinsignon, C. (2004) Lattice vibrations of manganese oxides. Spectrochimica Acta Part A: Molecular and Biomolecular Spectroscopy, 60(3), 689–700.

Kim, H., and Stair, P.C. (2004) Bacterially produced manganese oxide and todorokite: UV Raman spectroscopic comparison. Journal of Physical Chemistry B, 108, 17019–17026.

Kohler, T., Armbruster, T., and Libowitzky, E. (1997) Hydrogen bonding and Jahn-Teller distortion in groutite, α-MnOOH, and manganite, γ-MnOOH, and their relations to the manganese dioxides ramsdellite and pyrolusite. Journal of Solid State Chemistry, 133, 486–500.

Kong, K.P., Fischer, T.B., Heaney, P.J., Post, J.E., Stubbs, J.E., and Eng, P.J. (2019) Mineralogical and geochemical constraints on chromium oxidation induced by birnessite. Applied Geochemistry, 108, 104365.

Kwon, K.D., Refson, K., and Sposito, G. (2013) Understanding the trends in transition metal sorption by vacancy sites in birnessite. Geochimica et Cosmochimica Acta, 101, 222–232.

Lan, T., Tang, X., and Fultz, B. (2012) Phonon anharmonicity of rutile TiO₂ studied by Raman spectrometry and molecular dynamics simulations. Physical Review B, 85, 094305.

Le Goff, P., Baffier, N., Bach, S., and Pereira-Ramos, J.P. (1996) Synthesis, ion exchange and electrochemical properties of lamellar phyllomanganates of the birnessite group. Materials Research Bulletin, 31(1), 63–75.

Li, Z., Wang, J., Wang, Z., Ran, H., Li, Y., Han, X., and Yang, S. (2012) Synthesis of a porous birnessite manganese dioxide hierarchical structure using thermally reduced graphene oxide paper as a sacrificing template for supercapacitor application. New Journal of Chemistry, 36(7), 1490–1495.

Lopano, C.L., Heaney, P.J., and Post, J.E. (2009) Cs-exchange in birnessite: Reaction mechanisms inferred from time-resolved X-ray diffraction and transmission electron microscopy. American Mineralogist, 94, 816–826.

Manning, B.A., Fendorf, S.E., Bostick, B., and Suarez, D.L. (2002) Arsenic(III) oxidation and arsenic(V) adsorption reactions on synthetic birnessite. Environmental Science & Technology, 36(5), 976–981.

Marnocha, C.L. (2017) Rock coatings and the potential for life on Mars. Elements, 13, 187–191.

Marnocha, C.L., and Dixon, J.C. (2014) Endolithic bacterial communities in rock coatings from Kärkevagge, Swedish Lapland. FEMS Microbiology Ecology, 90, 533–542.

McKeown, D.A., and Post, J.E. (2001) Characterization of manganese oxide mineralogy in rock varnish and dendrites using X-ray absorption spectroscopy. American Mineralogist, 86, 701–713.

Nam, K.W., Kim, S., Yang, E., Jung, Y., Levi, E., Aurbach, D., and Choi, J.W. (2015) Critical role of crystal water for a layered cathode material in sodium ion batteries. Chemistry of Materials, 27, 3721–3725.

Northup, D.E., Snider, J.R., Spilde, M.N., Porter, M.L., van de Kamp, J.L., Boston, P.J., Nyberg, A.M., and Bargar, J.R. (2010) Diversity of rock varnish bacterial communities from Black Canyon, New Mexico. Journal of Geophysical Research: Biogeosciences, 115, 1–19.

Polák, L., Vlasáč, J., Vrtiška, L., and Mikuš, T. (2017) Cryptomelane, K(Mn₄⁴⁺Mn³⁺)O₁₆, from the Dúbravica-Zolnica Fe deposit (North Veporic Unit, Slovak Republic). Mineralia Slovaca, 49, 169–176.

Polverejan, M., Villegas, J.C., and Suib, S.L. (2004) Higher valency ion substitution into the manganese oxide framework. Journal of the American Chemical Society, 126, 7774–7775.

Porto, S.P.S., Fleury, P.A., and Damen, T.C. (1967) Raman Spectra of TiO₂, MgF₂, ZnF₂, FeF₂, and MnF₂. Physical Review, 154, 522–526.

Post, J.E. (1999) Manganese oxide minerals: crystal structures and economic and environmental significance. Proceedings of the National Academy of Sciences, 96(7), 3447–3454.

Post, J.E., and Bish, D.L. (1989) Thermal behavior of complex, tunnel-structure manganese oxides. American Mineralogist, 74, 177–186.

Post, J.E., Heaney, P.J., Cahill, C.L., and Finger, L.W. (2003a) Woodruffite: A new Mn oxide structure with 3 × 4 tunnels. American Mineralogist, 88, 1697–1702.

Post, J.E., Heaney, P.J., and Hanson, J. (2003b) Synchrotron X-ray diffraction study of the structure and dehydration behavior of todorokite. American Mineralogist, 88, 142–150.

Post, J.E., Von Dreele, R.B., and Buseck, P.R. (1982) Symmetry and cation displacements in hollandites: structure refinements of hollandite, cryptomelane and priderite. Acta Crystallographica, B38, 1056–1065.

Santelli, C.M., Webb, S.M., Dohnalkova, A.C., and Hansel, C.M. (2011) Diversity of Mn oxides produced by Mn (II)-oxidizing fungi. Geochimica et Cosmochimica Acta, 75, 2762–2776.

Shannon, R.D. (1976) Revised effective ionic radii and systematic studies of interatomic distances in halides and chalcogenides. Acta Crystallographica, A32, 751–767.

Shumlas, S.L., Singireddy, S., Thenuwara, A.C., Attanayake, N.H., Reeder, R.J., and Strongin, D.R. (2016) Oxidation of arsenite to arsenate on birnessite in the presence of light. Geochemical Transactions, 17, 5.

Tebo, B.M., Bargar, J.R., Clement, B.G., Dick, G.J., Murray, K.J., Parker, D., Verity, R., and Webb, S.M. (2004) Biogenic manganese oxides: properties and mechanisms of formation. Annual Reviews in Earth and Planetary Science, 32, 287–328.

Turner, S., and Post, J.E. (1988) Refinement of the substructure and superstructure of romanechite. American Mineralogist, 73, 1155–1161.

Xu, H.Y., Xu, S., Wang, H., and Yan, H. (2005) Characteristics of hausmannite Mn₃O₄ thin films by chemical bath deposition. Journal of the Electrochemical Society, 152, C803–C807.

Yang, L.F., Cheng, S., Ji, X., Jiang, Y., Zhou, J., and Liu, M.L. (2015) Investigations into the origin of pseudocapacitive behavior of Mn₃O₄ electrodes using in operando Raman spectroscopy. Journal of Materials Chemistry A, 3(14), 7338–7344.

Endnote:

[1]Deposit item AM-20-87390, Supplemental Material. Deposit items are free to all readers and found on the MSA website, via the specific issue's Table of Contents (go to http://www.minsocam.org/MSA/AmMin/TOC/2020/Aug2020_data/Aug2020_data.html).